Compressive Strength of Dry-Stacked Concrete Masonry Unit Assemblies

This paper contains a set of 124 tests on dry-stacked prisms completed to experimentally investigate the compressive strength of dry-stacked prisms using conventional concrete masonry units. The experiments account for the roughness at the bed joint, which is found to have a significant effect on the ultimate load-carrying capacity of the prism. Based on the experimental results, a unit strength evaluation standard is proposed for extending the current TMS 602-13.

Assessing the Compressive Behavior of Dry-Stacked Concrete Masonry with Experimentally Informed Numerical Models

This study assesses the behavior of dry-stacked prisms with ground and unground unit surfaces subjected to axial compressive loads. Experimentally validated and novel predictive models, that take the roughness at the bed joint into account, are used to study the prisms mechanical behavior under different untested scenarios and to develop mathematical relationships that describe this behavior and predict the prisms ultimate capacity. The prisms with unground units exhibit lesser ultimate capacity than prisms with ground units. Based on these results, look-up tables can be developed and implemented in future construction codes.

Experimental and Numerical Evaluation of Reinforced Dry-Stacked Concrete Masonry Walls

In this study, an experimentally validated finite element model is developed to study the mechanical behavior of dry-stacked concrete masonry walls subjected to out-of-plane loads. The ultimate load-carrying capacity and the failure patterns are studied for variations in material properties as well as configurations. Given that the walls can develop ductility, the findings of this study support the development of future design guides for dry-stacked construction systems.

Compressive Strength of Dry-Stacked Concrete Masonry Unit Assemblies

Sez Atamturktur, Ph.D., A.M.ASCE[1]; Brandon E. Ross, Ph.D., P.E., M.ASCE[2]; Jason Thompson, P.E.[3]; and David Biggs, P.E., S.E., Dist.M.ASCE[4]

Abstract: Dry-stacked masonry construction consists of individual units stacked directly without mortar at the bed and head joints. Although dry-stacked construction offers many benefits including speed of construction and minimal need for skilled labor, its use has been limited by lack of technical information. This paper presents the results of an experimental program investigating the compressive strength of dry-stacked assemblies built from nonproprietary standard concrete masonry units. The program included 124 tests of dry-stacked prisms; variables in the program included compressive strength of the units and treatment of the interface. Roughness of the interface was found to have significant effect on the load–displacement behavior and ultimate capacity of dry-stacked assemblies. Based on the experimental results, a unit strength method is presented for qualifying dry-stacked systems. **DOI: 10.1061/(ASCE)MT.1943-5533.0001693.**

Author keywords: Mortarless masonry construction; Unit strength method; Compressive strength; Ultimate capacity.

Introduction

Dry-stacked masonry construction consists of individual units stacked directly without mortar at the bed and head joints. Dry-stack masonry systems can be built with mechanically interlocked units, and be reinforced and/or prestressed (NCMA 2003). By omitting the mortar joints used in typical masonry construction, dry-stacked masonry can increase the speed of construction, reduce the effects of workmanship variability, minimize the need for skilled labor, and lower the construction costs (Ramamurthy and Kunhanandan Nambiar 2004; Ngowi 2005; Murray 2007; Hines 1992). Previous researchers have demonstrated that dry-stacked masonry can carry compressive loads similar to that of traditional masonry (Marzahn 1999; Marzahn and König 2002); however, the condition of the bed interface between units is critical to structural behavior and performance of dry-stacked systems (VanderWerf 1999; Jaafar et al. 2006). Proprietary interlocking systems have been the focus for the vast majority of dry-stacked masonry research (e.g., Drysdale 2000; Thanoon et al. 2007; Hamid 2004; Ngowi 2005; Pave 2007; Pave and Uzoegbo 2010). Lack of information on dry-stacked masonry has thus far been the primary limiting factor on its widespread use (Marzahn 1999; Biggs 2002). In particular, there is a dearth of information on the use of standard concrete masonry units (CMUs) in dry-stacked masonry.

The motivation for this paper is to help facilitate the use of standard CMU in grouted and reinforced dry-stacked walls. The paper presents the results of an experimental program conducted to evaluate the effects of different interface treatments on structural behavior and capacity of dry-stacked masonry using standard CMU. In dry-stack construction of masonry, the surface texture becomes an important factor governing the mechanical behavior of the assembly (Oh 1994; Jaafar et al. 2006). As a result, two interface-surface treatments were considered: ground and unground. The ground CMUs are smoothed with an abrasive cutting head to promote uniformity of the interface surfaces. Unground CMUs have rough surfaces and are used without any grinding or other modification. The test program involved compression tests of 124 dry-stacked masonry prisms; 61 with ground CMUs and 63 with unground CMUs. The other variable in the test program was the unit strength of blocks used in the prisms.

Technical contributions of this paper are twofold. First, distinctions in load–displacement behavior between ground and unground dry-stacked assemblies are elucidated. Second, recommendations are made for determining design values for the compressive strength of dry-stacked CMU systems based on surface condition and strength of the constituent units. To assist design practitioners, these recommendations are presented in the same format, and based on the same statistical approach, as the specification for masonry structures, TMS 602-13 (TMS 2013).

Background

Given the lack of dedicated design standards for dry-stack masonry construction, it is helpful to consider the quality control of masonry compressive strength as addressed in TMS 602-13 Section 1.4.B.2 (TMS 2013). This section presents two acceptable methods for verifying a given masonry system for compliance with the specified compressive strength of concrete masonry for mortared systems (f'_m). The first method, or *prism test method*, compares the specified compressive strength against the experimental strength of representative masonry prisms. The prisms are tested according to ASTM C1314 (ASTM 2011). The second and more commonly

[1]Distinguished Professor, Glenn Dept. of Civil Engineering, Clemson Univ., 109 Lowry Hall, Clemson, SC 29634 (corresponding author). E-mail: sez@clemson.edu

[2]Assistant Professor, Glenn Dept. of Civil Engineering, Clemson Univ., 109 Lowry Hall, Clemson, SC 29634. E-mail: bross2@clemson.edu

[3]Vice President of Engineering, National Concrete Masonry Association, 13750 Sunrise Valley Dr., Herndon, VA 20171.

[4]President, Biggs Consulting Engineering, 26F Congress St., #305, Saratoga Springs, NY 12866.

Note. This manuscript was submitted on August 17, 2015; approved on May 24, 2016; published online on August 31, 2016. Discussion period open until January 31, 2017; separate discussions must be submitted for individual papers. This technical note is part of the ***Journal of Materials in Civil Engineering***, © ASCE, ISSN 0899-1561.

Table 1. Unit Strength Method Table (TMS 602 2013, Reprinted with Permission of The Masonry Society, http://www.masonrysociety.org)

Net area compressive strength of concrete masonry [MPa (psi)]	Net area compressive strength of concrete masonry units [MPa (psi)]	
	Type M or S mortar	Type N mortar
11.72 (1,700)	—	13.10 (1,900)
13.10 (1,900)	13.10 (1,900)	14.82 (2,350)
13.79 (2,000)	13.79 (2,000)	18.27 (2,650)
15.51 (2,250)	17.93 (2,600)	26.44 (3,400)
17.24 (2,500)	22.41 (3,250)	28.96 (4,350)
18.96 (2,750)	26.89 (3,900)	—
20.69 (3,000)	31.03 (4,500)	—

Note: For units of less than 102 mm (4 in.) nominal height, use 85% of the values listed.

used method is the *unit strength method*. In the unit strength method, the net compressive strength of masonry is looked up in a table according to the type of mortar and compressive strength of the constituent units (Table 1). A given masonry system (mortar joints and masonry units) is in compliance as long as the strength value from the table is equal to or larger than the specified compressive strength used in design.

Table values for the unit strength method are based on compressive tests conducted by the National Concrete Masonry Association (NCMA 2012), and are the 75th percent confidence interval of the 10th percent lower bound of the test data. This approach results in an approximately 1% chance that compressive strength is lower than the table value (TMS 2013). The test program reported in this paper was conducted to develop a unit strength method for dry-stacked masonry. The test approach and statistical basis are consistent with the unit strength method in TMS 602-13 (TMS 2013).

Test Methods and Materials

A total of 124 prisms were tested in the program according to ASTM C1314 (ASTM 2011). Each prism consisted of two units stacked on top of each other and loaded to failure in compression (Fig. 1). The test machine used in the program had an integrated computer for monitoring and recording load and displacement. Displacement recorded by the system was the vertical displacement between the loading heads of the machine. This displacement corresponds to axial shortening of the specimens. Other data collected from each prism included cross-sectional area and failure description.

Variables in the test program included the strength of masonry units and the surface condition at the interface. Six different groups of prisms were tested. As presented in Table 2, each group had between 19 and 23 prisms and had a unique combination of strength and surface condition. All testing was conducted in the spring of 2015 at the National Brick Research Center of Clemson University in Anderson, South Carolina.

Unit strength was determined for the blocks in each group according to ASTM C140 (ASTM 2014b); a total of three tests were conducted for each group. According to ASTM C140 (ASTM 2014b), gypsum caps were placed on the top and bottom of each unit specimen and it is reasoned that the surface condition (ground or unground) did not affect the experimental unit strength.

CMUs for the program were donated by a regional masonry supply company. All units were in compliance with ASTM C90 (ASTM 2014a). Standard $204 \times 204 \times 406$-mm ($8 \times 8 \times 16$-in.) stretcher units were used in the program. For the ground units, the top and bottom surfaces were smoothed prior to testing. Smoothing consisted of grinding the top 1.6 mm (1/16 in.) off the top and bottom surfaces of standard block with an abrasive cutting head. Although grinding was applied to the top and bottom surfaces of the blocks in the test program, the procedure was the same as that used to create smooth-faced CMU (NWCMA 2005). Unground blocks were standard units and were not smoothed or otherwise modified. Surface conditions of the ground and unground specimens are shown in Fig. 2.

Roughness of the ground and unground blocks were compared using a modified version of ASTM E965 (ASTM 2015), commonly referred to as the *sand patch test*. This method is used to measure the texture depth (TD) of pavement and involves spreading sand to fill gaps in the pavement surface. The TD is equal to the volume of the sand required to fill the gaps divided by the area over which the sand is applied. In the case of the dry-stacked blocks, sand was applied over the area of the top surface. The ground blocks had a TD of 0.089 mm (0.0035 in.); unground blocks had a TD of 0.25 mm (0.010 in.).

Results and Discussion

Axial Stress-Strain Behavior

Representative stress-strain responses are shown in Fig. 3 for prisms with ground and unground units. These responses were calculated from the load, displacement, and geometric data collected during testing. Strain was calculated as the change in

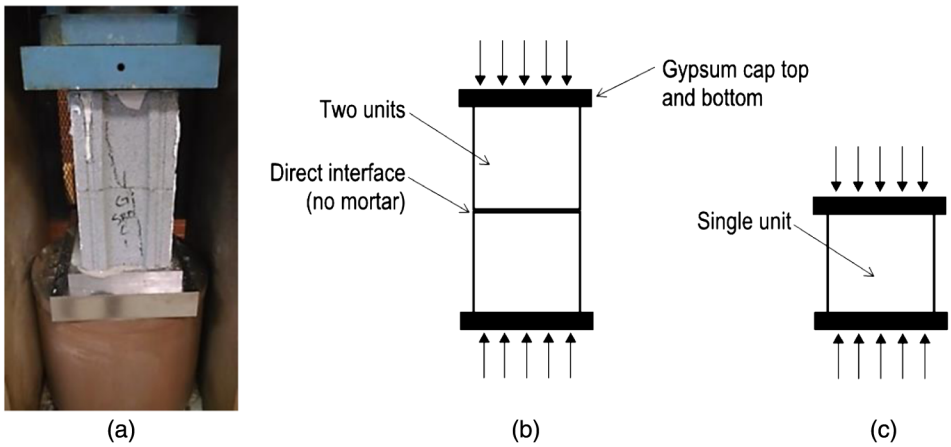

Fig. 1. Test specimens: (a) photo of prism in test machine; (b) schematic of prism specimen; (c) schematic of unit specimen

Table 2. Test Matrix

Tested unit strength [MPa (psi)]	Number of prism specimens
Ground units	
19.9 (2,880)	22
21.6 (3,140)	19
26.8 (3,890)	20
Unground units	
15.5 (2,250)	20
23.3 (3,380)	20
25.4 (3,680)	23

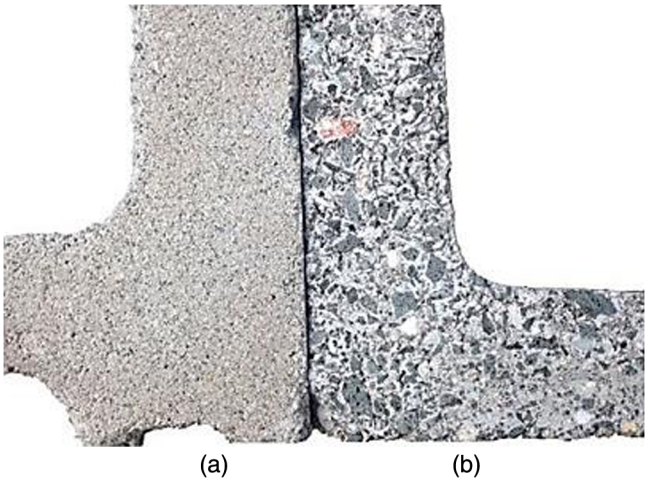

Fig. 2. Surface and interface condition of (a) unground; (b) ground specimens

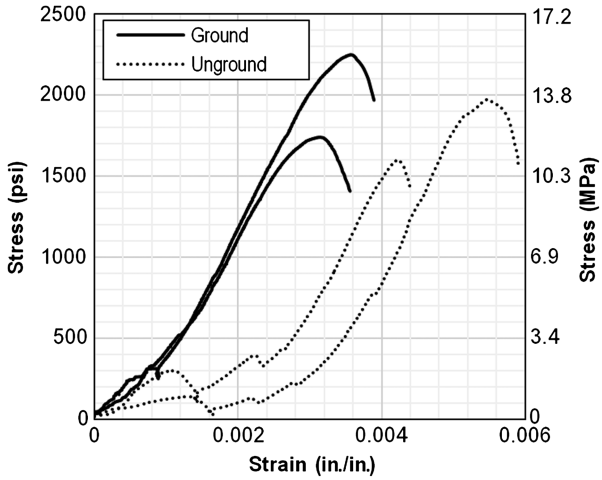

Fig. 3. Axial stress-strain response of representative prisms

position of the test machine loading heads divided by the height of the specimen. The datum, or *zero* position, that was used to calculate strain was taken as the position when the load first began to increase.

At lower loads, the stress-strain relationship in prisms with ground units was approximately linear. Stiffness of the ground prisms decreased with the onset of microcracking, which typically occurred at approximately 80% of peak stress. Large cracks formed at peak stress and the capacity decreased abruptly as the specimen broke into a small number (i.e., two or three) of large pieces.

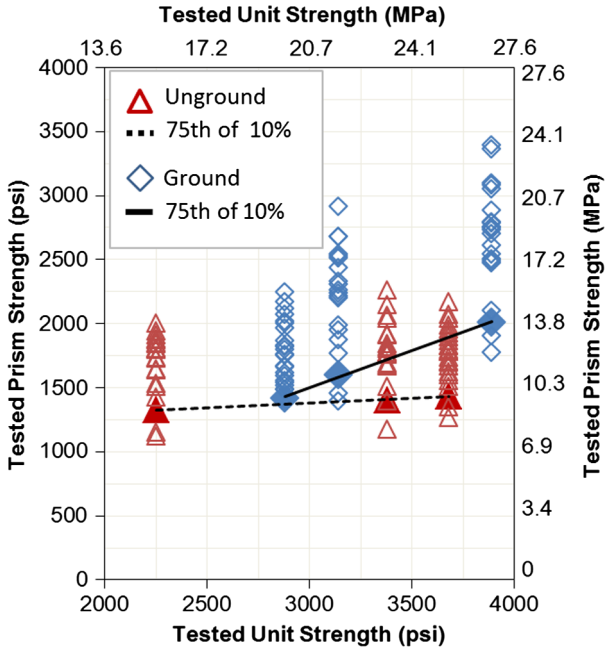

Fig. 4. Comparison of tested prism and unit strengths

Behavior of the prisms with unground units was distinct from those with ground units, particularly at lower loads. Abrupt changes in the stress-strain response occurred at low load levels. These abrupt changes are attributed to crushing of local *high spots* along the unground interface. A sudden drop in load accompanied local crushing, followed by an increase in load and stiffness as the compressive force was spread to a larger portion of cross section. This type of behavior is consistent with the *seating* behavior reported by Jaafar et al. (2006) and Thanoon et al. (2008). Stress associated with local crushing ranged from approximately 0.55 to 2.07 MPa (80 to 300 psi). Crushing continued until the strain reached between 0.002 and 0.003, at which point the stress and strain began to increase approximately linearly until the stress approached the peak level. At levels approaching peak stress, the behavior of prisms with ground and unground units was similar. However, unlike ground units, the unground units broke into a large number of small pieces.

Capacity

Prism and unit strength data are presented in Fig. 4. Best-fit linear trend lines are shown in the figures for the 75th percent confidence interval of the 10th percent lower bound. Each data point represents a single prism test. Compressive strength of prisms with ground units increased with increasing unit strength. On average, a 10% increase in unit strength resulted in an 8% increase in prism strength. By contrast, compressive strength of prisms with unground units was effectively constant regardless of unit strength. This distinction is attributed to local crushing of unground units; local crushing contributed to weakening of the prisms and did not allow the benefits of increased unit strength to be realized.

Unit Strength Method for Dry-Stacked Concrete Masonry

Table 3 is proposed for extending the current TMS 602-13 (TMS 2013) unit strength method to dry-stacked concrete masonry. As with the current method for traditional masonry (i.e., masonry with units and mortar), the proposed values are based on the 75th percent

Table 3. Compressive Strength of Dry-Stacked Masonry Based on Compressive Strength of Units and Type of Interface Condition

Net compressive strength of dry-stacked concrete masonry [MPa (psi)]	Net area compressive strength of masonry units	
	Ground units [MPa (psi)]	Unground units
9.00 (1,300)	NA	15.17–25.51 MPa (2,200–3,700 psi)
9.65 (1,400)	19.31 (2,800)	NP
11.03 (1,600)	21.72 (3,150)	NP
12.41 (1,800)	24.13 (3,500)	NP
13.79 (2,000)	26.54 (3,850)	NP

Note: NA = data not available; NP = not permitted.

confidence interval of the 10th percent lower bound. Small adjustments from the calculated values were made to round the proposed values down to the nearest 0.35 MPa (50 psi). As expected, compressive strength of masonry with ground units increases with increased unit strength. However, the compressive strength of masonry with unground units is consistent regardless of unit strength.

Comparing the proposed values for dry-stacked masonry (Table 3) with the current code values for traditional concrete masonry (Table 1), it is observed that for a given unit strength, the compressive strength is always lower for dry-stacked masonry. In addition, the range of unit strengths in Table 1 for traditional concrete masonry is greater than the range for dry-stacked masonry; additional data are required to extend the method to unit strengths greater than 26.54 MPa (3,850 psi) and less than 15.17 MPa (2,200 psi).

Summary and Conclusions

In this work, 124 masonry prisms were tested to determine the effects of unit strength and interface-surface condition on the compressive strength of dry-stacked masonry. Salient conclusions are as follows:

- Surface condition has significant effect on the stress-strain behavior of dry-stacked masonry. At low levels of stress, local high spots on the interface surface between unground units led to abrupt changes in stress-strain behavior of the test prisms. These abrupt changes were atypical in prisms with ground units.
- Compressive strength of dry-stacked concrete masonry with ground units increases as strength of the constituent units also increases. For prisms in the test program with ground units, a 10% increase in unit strength resulted in an average increase in prism strength of 8%.
- When using ground units, the net compressive strength of dry-stacked concrete masonry prisms is approximately 50% of the compressive strength of the units.
- Compressive strength of dry-stacked concrete masonry with unground units is effectively constant for varying levels of unit strength. In the test program, the compressive strength of prisms with unground units was unaffected by unit strength.

Acknowledgments

The authors acknowledge and thank the many organizations and individuals who contributed to the research presented in this paper. The research was funded by the National Concrete Masonry Association (Project NCMA 2014.001). Glenn Department of Civil Engineering students Seth Adams, Luay Abo Alarab, Marcos Martinez, and Michael Stoner participated in specimen preparation and testing. They were assisted by technical staff from the Glenn Department of Civil Engineering, Danny Metz, Scott Black, and Sam Biemann. Testing was conducted at the National Brick Research Center of Clemson University in Anderson, South Carolina. Masonry units were donated by the Oldcastle Company.

References

ASTM. (2011). "Standard test method for compressive strength of masonry prisms." *ASTM C1314*, West Conshohocken, PA.

ASTM. (2014a). "Standard specification for loadbearing concrete masonry units." *ASTM C90*, West Conshohocken, PA.

ASTM. (2014b). "Standard test methods for sampling and testing concrete masonry units and related units." *ASTM C140*, West Conshohocken, PA.

ASTM. (2015). "Standard test method for measuring pavement macrotexture depth using a volumetric technique." *ASTM E965*, West Conshohocken, PA.

Biggs, D. T. (2002). "Development of a mortarless post-tensioned masonry wall system." *Proc., 6th Int. Masonry Conf.*, British Masonry Society, London, 28–32.

Drysdale, R. G. (2000). "Properties of surface-bonded dry-stack block construction." Azar Group of Companies, Windsor, ON, Canada.

Hamid, A. (2004). "Development of a new loadbearing masonry wall system for building construction in hot climate." *Proc., 13th Int. Brick and Block Masonry Conf.*, Amsterdam, Netherlands.

Hines, T. (1992). "Using dry-stacked concrete masonry for affordable construction." *Proc., 4th Int. Seminar on Structural Masonry for Third World Countries*, Chennai, India.

Jaafar, M. S., Thanoon, W. A., Najim, A. M. S., Abdulkadir, M. R., and Ali, A. A. A. (2006). "Strength correlation between individual block, prism and basic wall panel for load bearing interlocking mortarless hollow block masonry." *Constr. Build. Mater.*, 20(7), 492–498.

Marzahn, G. (1999). "Investigation on the initial settlement of dry-stacked masonry under compression." *LACER No. 4*, Institute of Massivbau and Baustoff Technology, Leipzig Univ., Germany, 253–269.

Marzahn, G., and König, G. (2002). "Experimental investigation of long-term behavior of dry-stacked masonry." *J. Masonry Soc.*, 20(1), 9–21.

Murray, E. B. (2007). "Dry stacked surface bonded masonry—Structural testing and evaluation." M.S. thesis, Brigham Young Univ., Provo, UT.

NCMA (National Concrete Masonry Association). (2003). "Design and construction of dry-stack masonry walls." *TEK 14-22*, Herndon, VA.

NCMA (National Concrete Masonry Association). (2012). "Recalibration of the unit strength method for verifying compliance with the specified compressive strength of concrete masonry (MR37)." Herndon, VA.

Ngowi, J. V. (2005). "Stability of dry-stack masonry." Ph.D. thesis, Univ. of the Witwatersrand, Johannesburg, South Africa.

NWCMA (Northwest Concrete Masonry Association). (2005). "Specifying ground-face concrete masonry units." Lynnwood, WA.

Oh, K. (1994). "Development and investigation of failure mechanism of interlocking mortarless block masonry system." Ph.D. thesis, Drexel Univ., Philadelphia.

Pave, R. F. (2007). "Strength evaluation of dry-stack masonry." M.S. thesis, Univ. of the Witwatersrand, Johannesburg, South Africa.

Pave, R. F., and Uzoegbo, H. (2010). "Structural behavior of dry stack masonry construction." *Proc., SB10 Portugal: Sustainable Building Affordable to All: Low Cost Sustainable Solutions*, Algarve, Portugal.

Ramamurthy, K., and Kunhanandan Nambiar, E. K. (2004). "Accelerated masonry construction review and future prospects." *Prog. Struct. Eng. Mater.*, 6(1), 1–9.

Thanoon, W., Alwathaf, A., Noorzaei, J., Jaafar, M., and Abdulkadir, M. (2008). "Finite element analysis of interlocking mortarless hollow block masonry prism." *Comput. Struct.*, 86(6), 520–528.

Thanoon, W., Jaafar, M. S., Noorzaei, J., Razali, M., Kadir, A., and Fares, S. (2007). "Structural behavior of mortar-less interlocking masonry system under eccentric compressive loads." *Adv. Struct. Eng.*, 10(1), 11–24.

TMS (The Masonry Society). (2013). *Specification for masonry structures (TMS 602-13/ACI 530.1-13/ASCE 6-13)*, Longmont, CO.

VanderWerf, P. A. (1999). "Mortarless block systems." ⟨http://www.masonryconstruction.com⟩ (Aug. 10, 2016).

ASSESSING THE COMPRESSIVE BEHAVIOR OF DRY-STACKED CONCRETE MASONRY WITH EXPERIMENTALLY INFORMED NUMERICAL MODELS

Marcos Martínez[1], Sez Atamturktur[2], Brandon Ross[3], and Jason Thompson[4]

Abstract

In dry-stacked concrete masonry construction, units are laid without mortar, increasing the speed and reducing the cost of masonry installation. Despite these benefits, mortarless construction has not gained widespread acceptance as a viable alternative to traditional bonded masonry. This is largely attributed to the fact that the effect of surface roughness characteristics on the mechanical behavior of dry-stack masonry is not yet fully understood. To address this knowledge gap, the authors develop experimentally validated, predictive models that explicitly take the bed surface topography into account while representing the localized, nonlinear behavior at dry joints. With these validated models, a parametric analysis is completed to derive relationships between unit variables (e.g. material properties, surface roughness, grout strength) and the performance of mortarless prisms under axial compressive loads. The derived relationships contribute to the knowledge base in regards to the behavior of dry-stacked masonry construction.

Keywords: compressive strength, surface roughness, finite element modeling, contact elements, ASTM C140.

[1] Ph.D. Candidate, Dept. of Civil Engineering, Clemson Univ., Clemson, SC 29634
[2] Distinguished Professor, Dept. of Civil Engineering, Clemson Univ., Clemson, SC 29634 (corresponding author), E-mail: sez@clemson.edu
[3] Assistant Professor, Dept. of Civil Engineering, Clemson Univ., Clemson, SC 29634
[4] Vice President of Engineering, National Concrete Masonry Association, Herndon, VA 20171

1. Introduction

Laying concrete masonry units (CMU) dry without mortar, known as dry-stack construction, leads to significant reductions in construction time, the need for highly skilled labor, and construction cost (Oh 1994; Beall 2000; Ramamurthy and Nambiar 2004; Murray 2007). Such mortarless masonry systems have been shown to provide in-plane (Lourenço et al. 2005) and out-of-plane capacities (Ferozkhan 2005) provided by surface bonding and interlocking, capacities similar to conventional construction; however, they exhibit failure modes that are fundamentally different from those of bonded masonry. In conventional bonded masonry construction, the effects of irregular surface topography at the bed joints are mitigated by mortar. The absence of mortar in dry-stack construction, however, creates complex stress states with large gradients at the interface between the units. Local cracking and crushing resulting from these high stresses alter ultimate load capacity of the units (Jaafar et al. 2006) in a way that is not yet fully understood (Marzahn 1999; Anand and Ramamurthy 2000).

The contact behavior at the interface between the units depends on many micro-scale phenomena, including contact pressure, friction, and cohesion (Yastrebov et al. 2015). Previous studies on numerical modeling of mortarless masonry systems represented this interface with either zero-thickness contact (Baggio and Trovaluski 1993; Thanoon et al. 2007; Safiee et al. 2009) or two-dimensional link elements (Oh 1994; Campbell 2012), significantly simplifying the representation of the surface roughness. Recent studies have demonstrated that the actual variation in the height of the units (Thamboo and Dhanasekar 2015) as well as the surface topography influence the deformation in the contact area (Peng and Bhushan 2001; Jackson and Streator 2006, Thamboo et al. 2013). Hence, modeling the surface topography is essential for investigating the effect of the bed joint surface roughness on the stiffness characteristics, stress distribution and the

global behavior of the mortarless masonry system (Sellgren et al. 2003, Yastrebov et al. 2012). For instance, CMUs to be used in dry-stacked construction can have smoothed (ground) or rough (unground) bed surfaces (See Fig. 1 for microscale views of the bed surfaces of these two types of units), where the smooth bed surfaces are obtained using diamond-plated pads to grind the rough surfaces (following the same process used to create smooth face blocks), and the units with rough bed surfaces are those that are commonly provided by the manufacturers. The effect of such variation in bed surface roughness on the load carrying performance of dry-stacked systems is currently unknown, and studying this effect requires an explicit consideration of surface topography at the bed joint, which is precisely what is accomplished in this study.

In this paper, the authors present a modeling strategy for dry-stacked masonry systems that take into account not only the highly nonlinear behavior of the masonry material and the dry contact between the units but also the surface topography at the bed joint. A particular contribution of this paper is its focus on standard (8”×8”×16”) blocks (i.e. CMUs most commonly used in the United States), as past studies on this topic have primarily focused on proprietary units, often with interlocking components (Beall 2000; Anand and Ramamurthy 2005; Murray 2007; Pave 2007). The numerical models developed in this study for standard CMUs are rigorously compared against experimental measurements to validate their ability to yield accurate predictions regarding the influence of surface roughness on the global behavior of the prisms. The validated numerical models are then used to explore the relationship between the properties of standard CMUs and dry-stacked assemblies to better understand the behavior of this unconventional masonry construction technique.

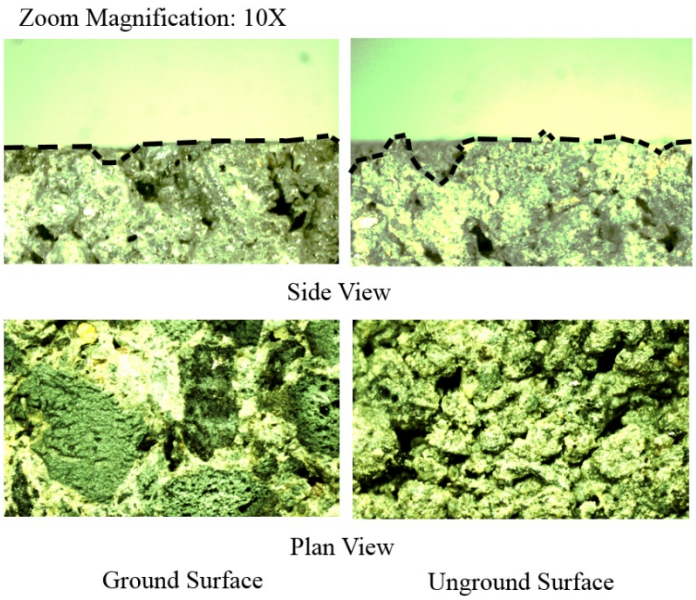

Fig. 1. The CMU bed ground (left) and unground (right) surface.

2. Numerical Models for Dry-stack Masonry Prisms

Finite Element (FE) models for two-unit dry-stack prisms with two variations, one each to represent smoothed (ground) or rough (unground) bed surfaces, are built in ANSYS v.15 (Fig. 2). These two models differ only in the contact surface between the units, built using the nominal dimensions of a two-core CMU, stretcher unit with an 8” width and height, a 16” length, a 1.25” thickness in face shells and a 1” thickness in end shell and web. Fillets at the edges in the cells and the tapering of the web are neglected to simplify the model geometry. The FE models are developed to include the top and bottom steel plates that are part of the universal testing machine. Boundary conditions at the base of the lower steel plate are fixed, restraining translation and rotation in all directions, while the top steel plate is restrained to prevent lateral movements (Fig. 3).

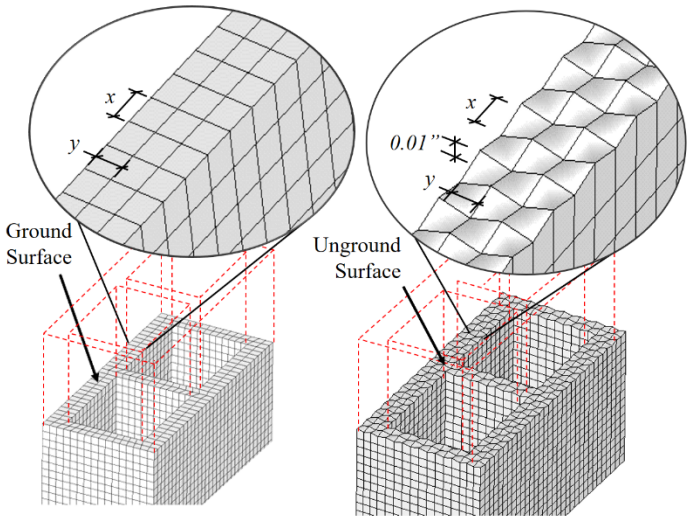

Fig. 2. FE models: Ground surface (left), unground surface (right); the vertical scale has been increased for enhanced visualization.

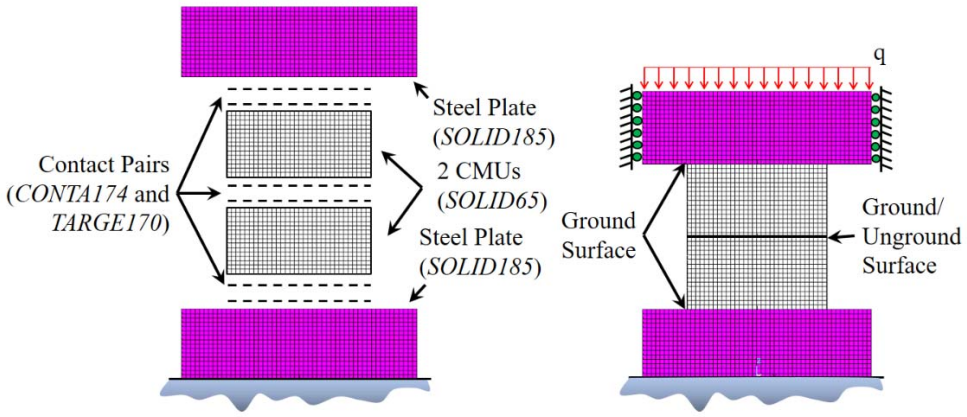

Fig. 3. FE model of the two-unit dry-stacked prisms, element types (left), the configuration during testing (right).

2.1 Element Type Selection and Material Model

ANSYS has the capability to represent the behavior of concrete masonry and grout with the specialized *SOLID65* element, a predefined 8-noded solid isoparametric hexahedron element that can simulate typical masonry failure, which is characterized by cracking in tension and crushing in compression (Truong-Hong and Laefer 2008; Lü et al. 2011). Steel plates of the

universal testing machine are represented with *SOLID185* elements, which have the capability to represent large deflection, large strain, and ductile materials (Salas and Sánchez 2012).

SOLID65 element accounts for cracking through a smeared crack analogy and crushing through a plasticity algorithm in three orthogonal directions according to the William–Warnke failure criterion (William and Warnke 1974; Fanning 2001). Failure occurs when multi-axial stresses in the element surpass the failure surface defined by the criterion. In particular, cracking and/or crushing occurs in the element at any integration point once one of the principal stresses lies outside the failure surface. After cracking occurs, the modulus of elasticity of the element at the integration point is set to zero in the direction parallel to the principal stress; however, a stiffness multiplier (0.6 as a default value) is applied at the integration point in the direction of the principal stress to ensure the convergence of the calculations. Similarly, after crushing occurs, the modulus of elasticity of the element at the integration point is set to zero in all directions of principal stresses; however, a stiffness multiplier (1.0E-06 as a default value) is applied at the integration point in the direction of the principal stress to avoid numerical instabilities (Dahmani et al. 2010).

SOLID65 element allows for the transfer of tangential loads across cracks, simulating the aggregate interlocking effect through the shear transfer coefficient for open cracks, and the interlock between cracked faces through the shear transfer coefficient for closed cracks (Parvanova et al. 2005; Contamine et al. 2011). This shear transfer coefficient ranges from 0.0 to 1.0, where 0.0 represents a perfectly smooth crack (complete loss of shear transfer capability), and 1.0 represents a perfectly rough crack (no loss of shear transfer capability). The coefficients are often set for open and closed cracks independently. This study adopts shear transfer coefficients used in

previous studies of 0.2 for open cracks and 0.6 for closed cracks (Kachlakev et al. 2001; Prabhu et al. 2014).

To account for the plasticity prior to cracking and/or crushing, the Drucker-Prager model (Drucker et al. 1952), yield criterion widely implemented for masonry structures is adopted (Sayed-Ahmed and Shrive 1996; Michel 2015; Stefanou et al. 2015). This criterion defines a surface created in the principal stress domain that takes into account the limited plastic-flow ability before crushing. This yield criterion introduces an elastic perfectly plastic model that is defined by two parameters: cohesion c and the internal friction angle ϕ. Values $\phi = 36.65^\circ - 1.1^\circ (f'_{unit}/1000)$ proposed by Dahl (1992) and Mahboubi and Ajorloo (2005) and $c = f'_{unit}/4$ proposed by Chen (1982) are adopted here, and the values $\phi = 0.01 f'_{grout}$, and $c = 0.129 f'_{grout} + 268.32$, proposed by Köksal et al. (2005), are used to represent the grout. The measured averaged properties of individual concrete masonry units (e.g., compressive strength and modulus of elasticity) are listed in Table 1 along with other properties recommended in the literature needed to define the material model in the numerical model.

Table 1. Material properties of the units and grout specimen entered into the FE model.

Material Properties	Ground Units			Unground Units			Grout
Measured in the laboratory	G1	G2	G3	U1	U2	U3	GG
Modulus of elasticity (ksi)	792	1,075	1,817	600	1,180	1,400	2,200
Compressive strength, f'_{unit} (psi)	2,857	3,140	3,263	2,188	2,511	3,675	4,400
Obtained from literature (see *Element Type Selection and Material Model* Section for details)							
Poisson's ratio	0.2	0.2	0.2	0.2	0.2	0.2	0.2
Cohesion, c (psi)	719	785	816	547	628	919	836
Friction angle, ϕ (°)	33.5	33.2	33.1	34.2	33.9	32.6	44
Tensile strength, f_t (psi)	288	314	326	219	251	368	440
Shear transfer coef. for open cracks, β_t	0.2	0.2	0.2	0.2	0.2	0.2	0.2
Shear transfer coef. for closed cracks, β_c	0.6	0.6	0.6	0.6	0.6	0.6	0.6

2.2 Representation of Dry-stack Contact Stiffness

For the prism with unground units, a rough surface is assumed at the contact between units. Rough surfaces are composed of a large number of asperities (or peaks and valleys). To model the roughness, the prisms include gaps between the two units but with contact occuring at the peaks (high points). Three parameters describe the asperities: length (x), width (y) and peak height or depth (Recall Fig. 2). The asperities are created by moving a predefined set of nodes in the mesh hence by changing the aspect ratios of the individual finite elements. The mesh size in the model is set according to the x and y asperities. The asperity height is assumed to be uniform at the mean height texture depth of 0.01" and is determined using the sand patch test (see ASTM E965 and ASTM 2015). The sand patch test measures the texture depth of a rough surface and involves spreading sand to fill gaps in the surface. The texture depth is equal to the volume of the sand required to fill the gaps divided by the area over which the sand is applied (Atamturktur et al. 2016). For the prism with ground units, the bed surface is kept smooth (Fig. 2 left). Both variations of FE models include 31,340 nodes and 27,792 elements.

The interfaces between CMU and steel plate, as well as CMU and CMU are modeled with 8-node contact elements *CONTA174* and *TARGE170*. In the numerical model, the contact interface

is modeled using the contact (*CONTA174*) and target (*TARGE170*) surfaces available in ANSYS. The contact and target surfaces constitute a contact pair that can identify when contact occurs and prevent (or limit) penetration between the solids (Recall Fig. 3). The contact pair supplies a scheme for ensuring a proper transfer of forces between two solids according to normal and tangential contact stiffnesses. In this study, the normal contact stiffness, which controls the penetration between the two bodies, is assumed to be identical to the stiffness of the body beneath the contact element. The tangential contact stiffness, used to represent the sliding behavior, is idealized via the coefficient of friction (Prabhu et al. 2014).

Sliding behavior of the contact pair is governed by the Mohr-Coulomb criterion given as $\tau_{lim} = \mu\sigma + c_c$, where τ_{lim} represents the limit for shear stress at which sliding begins, σ represents the normal contact pressure, μ represents the coefficient of friction, and c_c represents contact cohesion. When the shear stress exceeds τ_{lim}, the elements *CONTA174* and *TARGE170* allow sliding. In contact surfaces, cohesion can provide sliding resistance; however, because contact cohesion is negligible at dry joints ($c_c = 0$), the shear stress is carried entirely by the friction (Vasconcelos and Lourenço 2009). In both variations of the FE models, the coefficient of friction is set to be 0.3 between CMU-CMU and 0.15 between CMU-steel plates (Gorst et al. 2003).

The contact between the surfaces generates a nonlinearity; a change in stiffness occurs in the contact between two solid bodies as a function of the nodal displacements. The contact nonlinearity arises when one body tries to penetrate another solid body. The penetration must be within tolerances to have a converged solution. Although many formulations exist for solving contact problems (Laursen 2003), the Augmented Lagrange method (Bertsekas 1996) is preferred for modeling the prism with ground units. This is because the method is capable of controlling penetration at the contact surface by introducing an opposing force at the nodes at which contact

is detected. For the FE model for the prism with unground units, the Multi-point Constraints method (Ainsworth 2001) is preferred as this method satisfies the impenetrability between the unground surfaces. Unlike the Augmented Lagrange method, Multi-point Constraints uses rigid constraint equations between the solid elements on the contact and target elements, eliminating degrees of freedom at the nodes on the contact and target elements (Cunningham 2014).

2.3 Laboratory Experiments to Determine Concrete Masonry Unit Properties

To determine the unit properties (i.e. compressive strength and modulus of elasticity) needed for the development of the FE models, individual units are tested according to ASTM C140 (ASTM 2014). Table 2 shows the results obtained from 18 units categorized according to different compressive unit strengths per manufacturer specifications (G1 to G3 and U1 to U3). This table also shows the range of the measured compressive strength (f'_{unit}) for all three replicates. Grout used to fill the cores (GG) is also tested in accordance with ASTM C476 (ASTM 2016a) and ASTM C1019 (2016b). In the absence of tensile test data, the tensile strength (f'_t) is approximated to be about 10% of the compressive strength (Klingner 2010). The modulus of elasticity is derived from these measurements according to ASTM E111 (ASTM 2010) as the chord modulus of the predominantly linear region of the stress-strain curve. In our application, this coincides with the region between 50% and 80% of the ultimate strength.

Table 2. Unit properties measured by testing.

Unit Type	Category	# of Tests	Specified Unit Strength	Measured Strength		Measured Elasticity	
				Min.	Max.	Min.	Max.
Ground Units	G1	3	2,000	2,689	2,970	668,543	926,180
	G2	3	2,500	2,962	3,234	953,907	1,228,408
	G3	3	3,000	3,107	3,432	1,710,043	1,945,075
Unground Units	U1	3	2,000	1,893	2,397	560,439	643,679
	U2	3	2,500	2,413	2,741	1,050,670	1,269,420
	U3	3	3,500	3,247	3,974	1,270,643	1,501,424
Grout Specimens	GG	2	-	4,320	4,480	2,078,406	2,321,594

Note: Units are in psi.

2.4 Numerical Solution Set-up and Mesh Refinement Study

The dry-stack prism behavior under compression is simulated considering both self-weight and the static vertical compressive pressure (*q,* in Fig. 3*).* Pressure applied on the upper surface of the steel plate is increased until failure is reached in the prism. Obtaining converged numerical solutions is challenging for this problem due to the combined effects of material nonlinearity (concrete cracking and crushing) and nonlinear boundary conditions at the contact surfaces. The FE model is solved using the iterative Newton-Raphson algorithm (Madenci and Guven 2015), tracing the equilibrium path during the load-deformation response. The Newton-Raphson scheme updates the tangent matrix and the restoring force vectors analogous to the element internal forces (Bathe 1996; Prabhu et al. 2014; Subramani et al. 2014).

The localized nonlinear behavior that involves cracking and crushing of the material makes it crucial to evaluate the adequacy of the mesh size to yield accurate solutions. The authors used the Grid Converge Index (GCI) to quantify the order of convergence and the bounds for discretization error (Roache 1994; Schwer 2008; Atamturktur 2009; Kwasniewski 2013). GCI is based on a generalized Richardson Extrapolation using the responses obtained with three mesh sizes ($\Delta_F=0.5$ in., $\Delta_M=1$ in., and $\Delta_C=2$ in.). The GCI value is calculated as $GCI=(F_S\varepsilon)/(R^p$-

1)×100%, where F_S is a factor of safety with a suggested value of 1.25 when three mesh sizes are evaluated; ε is the difference between subsequent solutions for a group of meshes (i.e., fine (Δ_F) to medium (Δ_M) and medium (Δ_M) to coarse (Δ_C)) at each load stage; R denotes the refinement ratio, which is the ratio of mesh sizes; and p denotes the rate of convergence. The rate of convergence can be estimated through Eq. 1.:

$$p = \frac{log\left(\frac{y(\Delta_M)-y(\Delta_C)}{y(\Delta_F)-y(\Delta_M)}\right)}{log\, R} \qquad \text{Eq. 1.}$$

where $y(\Delta_x)$ is the discrete solution for displacements of the different mesh sizes. When the rate of convergence is estimated using the group from fine (Δ_F) to medium (Δ_M) or from medium (Δ_M) to coarse (Δ_C), a rate of convergence value of approximately $p=1$ is obtained, indicating first-order convergence as $\Delta_x \rightarrow 0$. This matches the first-order of accuracy of the 8-noded *SOLID65* element, indicating the suitability of the evaluated mesh sizes. Finally, the results of the mesh refinement study show a value of 2.13% for and 4.18% for $GCI_{M\text{-}C}$. The value obtained for $GCI_{F\text{-}M}$ results in a numerical uncertainty that is sufficiently lower than the experimental variability; therefore, the fine mesh size (i.e., 0.5 in.) is deemed appropriate.

3. Experimental Validation of FE Models

The response of two-stack mortarless masonry prisms under compressive loads are experimentally measured and compared against the predictions of the developed FE models. The experimental campaign involved two-unit dry-stacked, prisms built with units that had ground and unground bed surfaces. Two distinct types of model response are compared with experiments: the failure pattern, which is evaluated through a visual comparison, and the ultimate compressive strength of the prisms, which is evaluated quantitatively considering the experimental variability.

3.1 Hollow and Grouted Prism Tests

A total of 124 prisms are built by dry-stacking two standard 8”×8”×16” units (half of which are built with ground units and the other half with unground units). The compressive strength of the prisms is determined according to ASTM C1314 (ASTM 2011) using a SATEC Systems M11-400RD universal testing machine (Fig. 4).

Fig. 4. Experimental setup for prism masonry test.

Fig. 5 compares two representative prisms with ground and unground units. At ultimate compressive strength, the prism with unground units exhibits significantly larger deformations (strain of 0.53%) than the prism with ground units (strain of 0.33%). For grouted prisms, four specimens are built, two with ground units and two with unground units. The grout is poured in the cells, tamped with a metal rod, and finished to a smooth, level surface. The experimental test includes procedures for providing plane surfaces on the two bearing surfaces of the prisms through capping according to ASTM C1552 (ASTM 2016c).

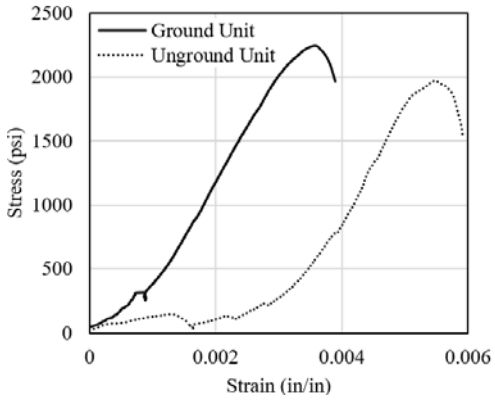

Fig. 5. Representative stress–strain curve for prisms with ground and unground units.

3.2 Test-Analysis Comparison

3.2.1 Failure Patterns

Failure patters are experimentally observed and numerically predicted failure patterns are compared for hollow prisms with ground units for the G1 category as shown in Fig. 6. Model predictions agree with experimental observations in that cracking initiates at approximately 80% of the ultimate load near the top and bottom corners of the ground units. It extends diagonally across the end shells and propagates along the height (Fig. 6). Fig. 7 depicts the stress-strain diagrams obtained from compressive tests conducted on 22 nominally identical hollow prisms with ground units (i.e., G1 category). The scatter in the stress-strain plots can be explained by the inherent variability in the dry-stacked bed joints as well as the unit-to-unit variations in material properties, which could collectively lead to different failure mechanisms for the prisms. Indeed, during the 22 replication tests, different failure patterns are observed in the experiments; the most frequently observed failure pattern is presented in Fig. 7.

However, in both the experimental observations and the model predictions, cracking initiates in the face shell when the load reaches approximately 90% of the ultimate load. Cracks at the corners of the units start to propagate diagonally across the face shell, forming an X shape, at which point severe crushing occurs across the contact area between units. The calculated

compressive strength at failure is considered to be the load at which a considerable number of solid elements have cracked and/or crushed; beyond this load, rigid body motion governs the behavior. The post-peak response of the dry-stacked prisms is omitted due to the issues regarding numerical instability. Thus, the simulation is terminated at the ultimate load.

Also, Figs. 7 and 9 show a seating effect (Oh 1994; Kaushik et al. 2007; Andreev et al. 2012; MSJC 2013; Lin et al. 2015), especially in the experiments of prism with unground units at compressive stresses less than 300 psi (Recall Fig. 5). In this study, the elastic perfectly plastic Drucker-Prager (DP) material model that takes into account plastic deformations is implemented to simulate the ultimate compressive behavior of dry-stacked prisms. When it is desired to represent the seating effect with the FE simulation, one could implement a multilinear elastic material (MLE) model. It is, however, important to note that the DP model is 30% more computationally efficient than the MLE, and as evidenced in the stress-strain plots of Figs. 7 and 9, both models converge to approximately similar ultimate compressive strengths.

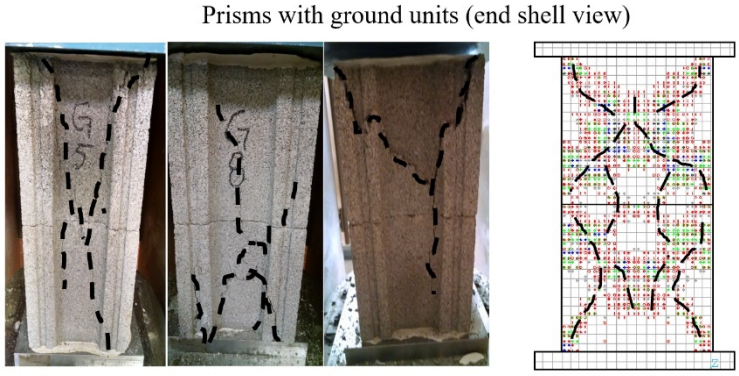

Fig. 6. Cracking/crushing pattern comparison in the end shell between experiments and numerical model for hollow prisms with ground units.

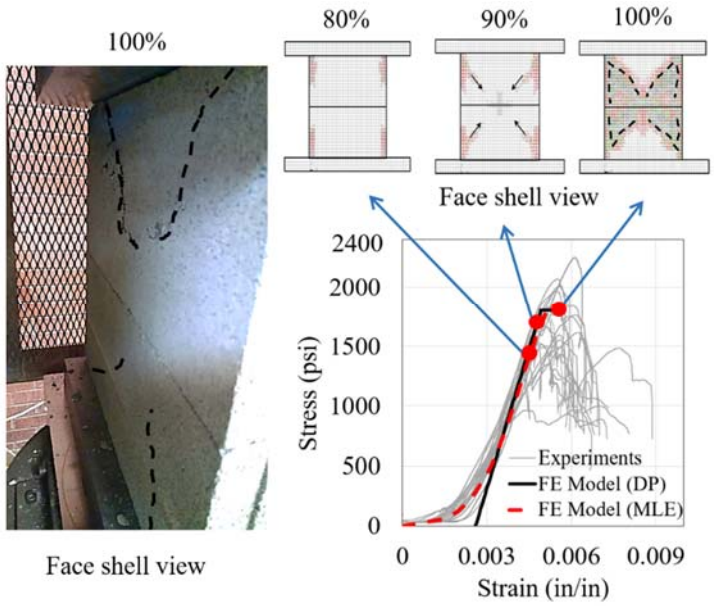

Fig. 7. Cracking/crushing pattern comparison in the face shell between experiments and numerical model for hollow prisms with ground units.

The same comparative study is repeated for prisms with unground units as shown in Fig. 8 for the UG1 category. Both the experiments and the numerical model show a concentration of stresses in the dry contact surface, and crushing initiates at early load stages in the contact area. The end shell exhibits vertical cracking that begins at the contact area and propagates along the height when the load reaches approximately 70% of the ultimate load. Fig. 9 shows a comparison of the failure pattern in the face shell observed during the experiments to that predicted by the FE model. In both the experiments and the numerical models, when the load reaches 75% of the ultimate load, cracks in the face shell at the unit interface propagate up and down from the corners at a 45-degree angle. Through the test-analysis comparison presented in Fig. 6-9, the numerical model is deemed to be capable of providing a representative failure pattern of the experimental tests.

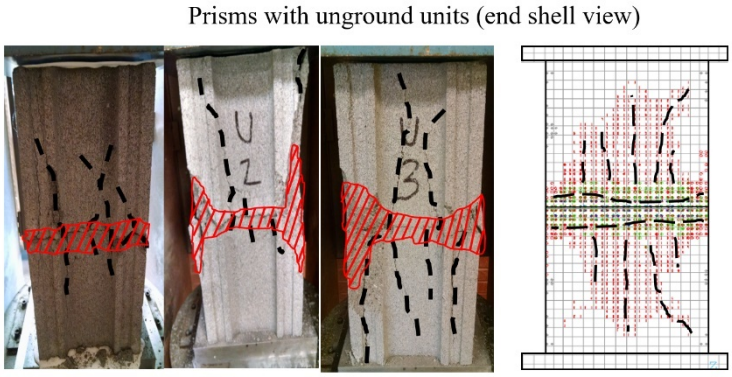

Fig. 8. Cracking/crushing pattern comparison in the end shell between experiments and numerical model for hollow prisms with unground units.

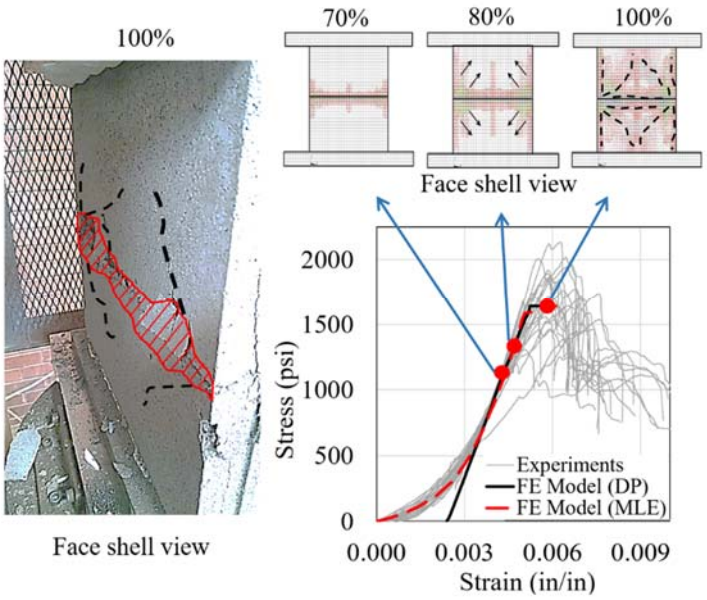

Fig. 9. Cracking/crushing pattern comparison in the face shell between experiments and numerical model for hollow prisms with unground units.

Fig. 10 shows the failure pattern in the face shell of grouted prisms with ground and unground units (i.e., the GG+G1 and GG+U1 categories). From the figure, a diminished seating effect can be seen in the experiments in grouted prisms. This observation applies to both ground and unground units. The failure pattern in prisms with both ground and unground units exhibits an X

shape across the height of the prism. However, a stress concentration around the bed joint in the grouted prisms with unground units is still noticeable.

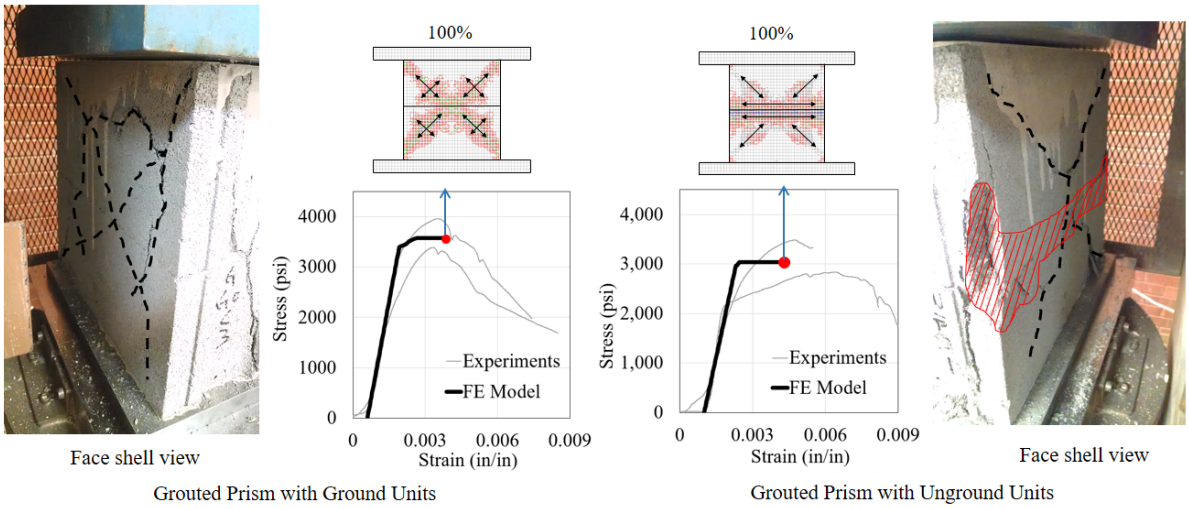

Fig. 10. Cracking and/or crushing pattern within the face shell of grouted prisms observed in the experiments and calculated by the numerical model (left) prisms with ground units and (right) prisms with unground units.

3.2.2 Ultimate Compressive Strength

The experimental measurements and the corresponding model predictions for the prisms under compressive load are compared in Table 3. The differences between ultimate compressive strength values measured for the prisms built with ground and unground units and their corresponding FE models are within the range of experimental variability. The compressive strength of the prisms predicted by the FE model is within the range of variability of the prism compressive strength measured during the experiments. Thus, the comparison of the experimental prism tests and the FE model predictions indicates that the developed models are an adequate representation of mortarless masonry behavior.

Table 3. Comparison of measured and calculated prism response.

Unit Type	Category	Measured Strength		Calculated Strength	Within Range?
		Min.	Max.		
Ground	G1	1,643	1,909	1,805	Yes
	G2	1,990	2,458	2,235	Yes
	G3	2,444	2,932	2,629	Yes
Unground	U1	1,541	2,053	1,647	Yes
	U2	1,461	1,939	1,706	Yes
	U3	1,605	1,971	1,953	Yes
Grouted	GG+G1	3,390	3,954	3,574	Yes
	GG+U1	2,837	3,484	3,038	Yes

Note: Units are in psi.

4. Parametric Study of Prism Strength

One of the main purposes of a validated numerical model is to predict the response of the system at untested settings or configurations. Here, the FE models of the prisms are executed to predict the ultimate compressive strength of the dry-stacked prisms for varying unit strength, grout strength, surface roughness, and unit dimensions through a parametric analysis.

4.1 The Effect of Unit Strength

To derive a functional relationship between the unit compressive strength (f'_{unit}) and prism strength, the latter is numerically evaluated for varying values of the former. During this evaluation, the modulus of elasticity and the unit tensile strength (f'_t) are varied with respect to the compressive strength. The modulus of elasticity is defined as 900 times the compressive strength of the unit (MSJC 2013), while the tensile strength is defined to range from 10% to 20% of the ultimate compressive strength (Drysdale et al. 1994). The results are obtained for prisms built with ground and unground units, as illustrated in Fig. 11. As seen in this figure, both prisms exhibit similar near-linear relationships between unit and prism strength; however, prisms with unground units exhibit approximately 15% less strength capacity compared to prisms with ground units.

When the ratio between unit tensile and compressive strengths increases in increments of 2% (i.e., tensile strength = 10, 12, 14,…20% of compressive strength), the ultimate capacity of the prisms increases by 7-11% for prisms with ground units and by 8-12% for prisms with unground units. The response of both hollow prisms with ground and unground units can be predicted through Eq. 2 and Eq. 3, respectively, where a valid domain for f'_{unit} is from 2,000 psi to 3,750 psi and for f'_t is from $0.1f'_{unit}$ to $0.2f'_{unit}$.

$$f'_{prism} = 402 + 0.16f'_{unit} + 3.4f'_t, \quad \text{Eq. 2}$$

$$f'_{prism} = 248 + 0.14f'_{unit} + 3.2f'_t, \quad \text{Eq. 3}$$

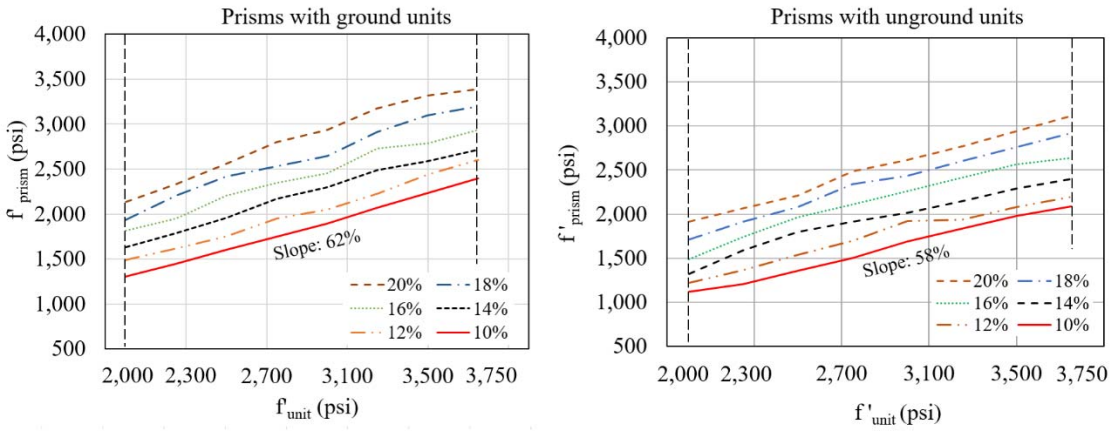

Fig. 11. Predictions for different tensile strengths as percentages of compressive strength for the prisms with ground (left) and unground (right) units.

4.2 The Effect of Surface Roughness

Another parameter of interest is the surface roughness of the units at the bed joint. Assuming a periodic distribution of asperities, this effect is evaluated through a roughness index (RI) defined as N_v/N_p, where N_v and N_p are the number of nodes that form the valleys and the peaks, respectively (see Fig. 12). For RI=1, there is only one node in the mesh creating the valley; for RI=2, there are two nodes creating the valley, and so on. All the models discussed previously were simulated using an RI=1, meaning that surface roughness was represented as a continuous

series of peaks and valleys with equal widths (the widths were defined by the mesh size). In this parametric study, N_p is fixed to 1 (i.e., RI=1 is a rougher surface). Fig. 12 shows that the relationship between unit and prism strengths is nearly linear for all three values of RI. With a higher RI, there are fewer peaks in the contact area between units. As a result, the prism strength increases as the RI value increases approaching a behavior similar to prisms with ground units. As the compressive load increases, the gap between the two units at the bed joint due to the asperities is gradually closed. At higher values of RI (i.e., smaller number of peaks), the initial gap closes at lower load levels, increasing the contact area between units. As a result, the stress distribution in the bed joint becomes more uniform in the valleys at lower load levels than the prisms with lower RI values. This helps reduce the extent of local failures around the peaks and allows for an increase in the load-carrying capacity of the prism.

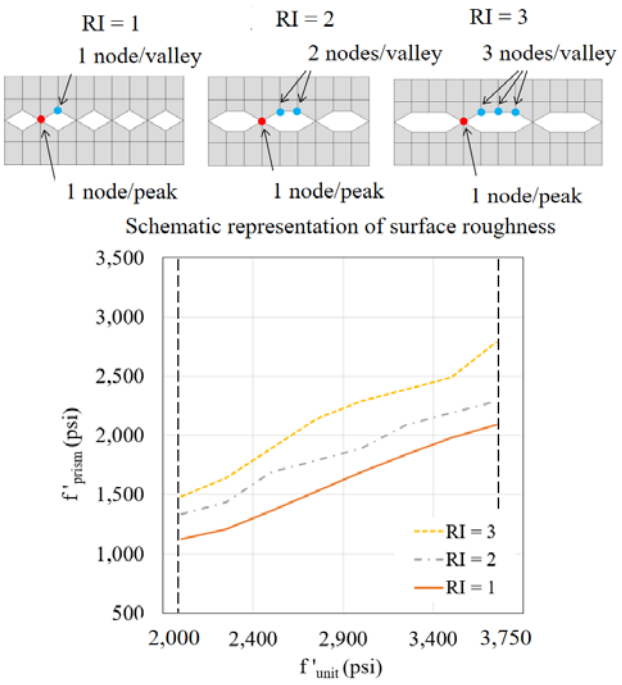

Fig. 12. Predictions of compressive strength of prisms with unground units at different RI.

4.3 The Effect of Unit Size

The effect of unit size is investigated for two-core hollow units ranging from 6” to 12” in depth, all of which are widely available commercial CMUs in the United States. Fig. 13 depicts an increase in the ultimate load capacity of the prism (F_{prism}) as the unit size increases, and Eq. 4 supplies an empirical representation of this increase using shape factors (i.e., a, b, and c that are given in Fig. 13).

$$F_{prism} = a + bf'_{unit} + cf'_{prism\,8"}, \qquad \text{Eq. 4}$$

Fig. 14 shows the lateral and axial stress distributions at the face shell along the height of the two types of prisms for different unit sizes at the same load level. However, there is no appreciable difference in the *shape* of stress distribution in that a high concentration of stresses is visible in the contact area between units, indicating a consistent behavior under axial loads for all unit dimensions studied.

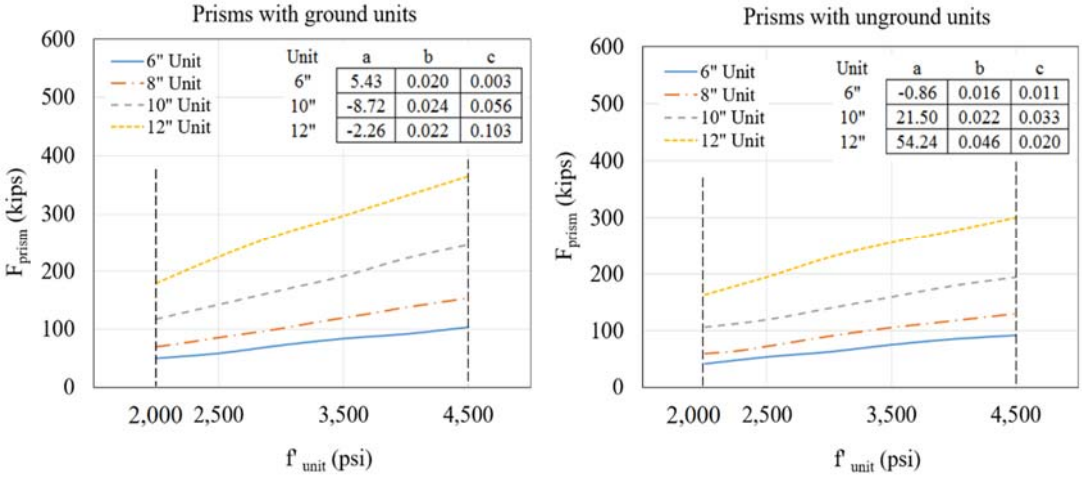

Fig. 13. Plots of ultimate force on the prisms for different unit sizes as a function of the compressive strength of ground (left) and unground (right) units.

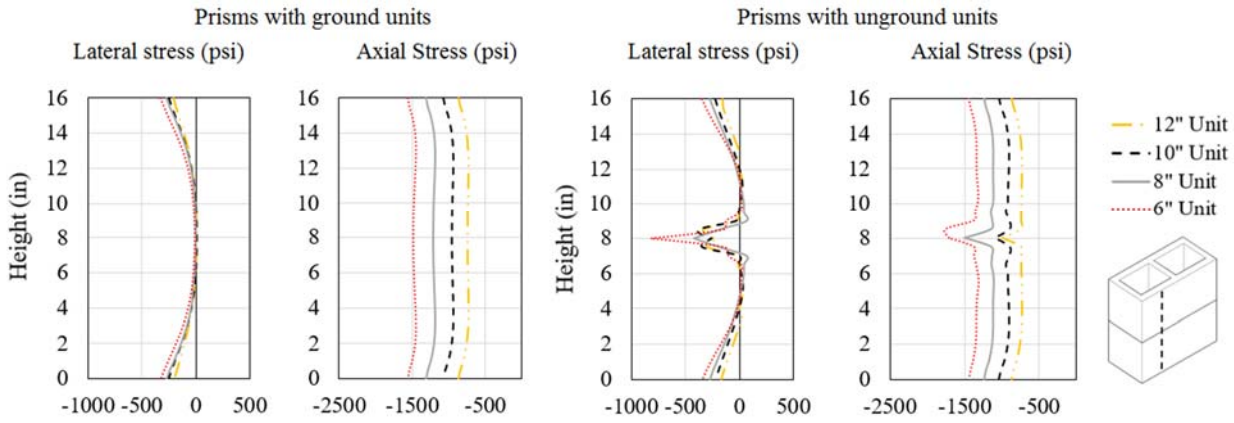

Fig. 14. Lateral and axial along the height of prisms with ground (left) and unground (right) units at the same load level.

4.4 The Effect of Grouting

To compare the differences in the performance of units with and without grout, the prisms shown in Fig. 15 are evaluated with full grout (with a grout compressive strength of 4310 psi and a modulus of elasticity of 2E+6 psi). Grouted prisms are built with the assumption of perfect bond at the interfaces between units and grout, and continuity of grout along the prism height. The results show that for both prisms with ground and unground units, the contribution of the grout to the ultimate compressive strength of prisms is independent of the unit strength. Grout contributes to the ultimate capacity by approximately 1730 and 2000 psi for prisms with ground and unground units, respectively. The ultimate strength of the grouted prisms, however, is nearly identical regardless of whether ground or unground units are used. Different grout strengths are simulated and give similar results. Thus, grouting is observed to diminish the differences in the strength between prisms with ground and unground units. The response of the grouted prisms with ground and unground units can be predicted through Eq. 5 and Eq. 6, where a valid domain for f'_{unit} is from 2,000 psi to 3,750 psi, and for f'_{grout} is from 2,000 psi to 4,500 psi.

$$f'_{prism} = 346 + 0.5f'_{unit} + 0.43f'_{grout}, \quad \text{Eq. 5}$$

$$f'_{prism} = 167 + 0.46f'_{unit} + 0.46f'_{grout}, \quad \text{Eq. 6}$$

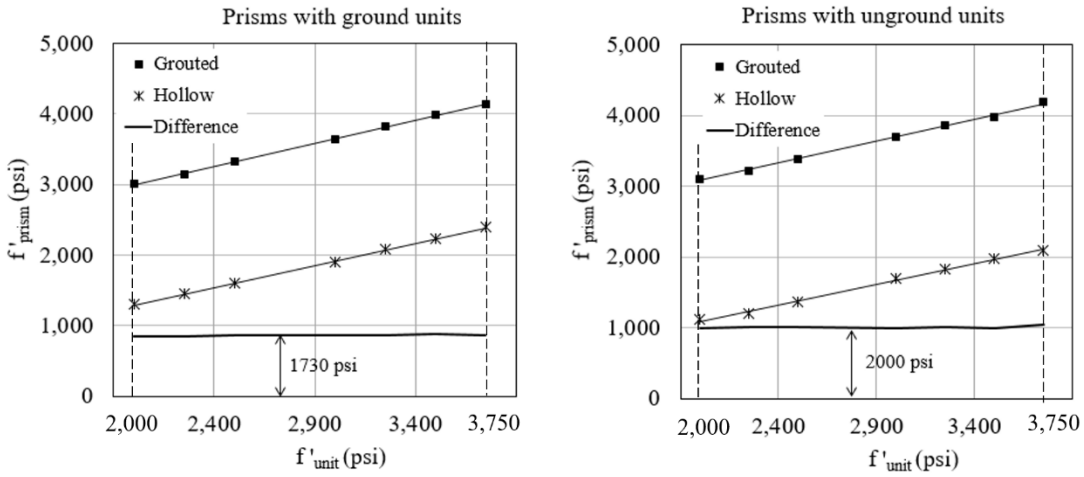

Fig. 15. Compressive strength for the hollow and grouted prisms with ground (left) and unground (right) units.

Stress distributions across the height of the face shell for hollow and grouted prisms are compared in Fig. 16. This figure also compares the behavior of prisms built with ground and unground unit surfaces. For prisms with ground units, the axial stress distribution before failure is highly uniform; however, for prisms with unground units, a stress concentration in the contact area is noticeable. Stress distribution across the height of the end shell before and after failure is shown in Fig. 17 for both hollow and grouted prisms with ground and unground units. In grouted prisms, the axial load laterally expands the grouted core and thus pushes the face shell outward due to the triaxial stress state of the grout. The axial stress is nearly uniform across the height of prisms with ground units; however, for prisms with unground units, there is a stress concentration in the contact area between units. For lateral stresses, there is again a concentration in the contact area for prisms with unground unit surfaces.

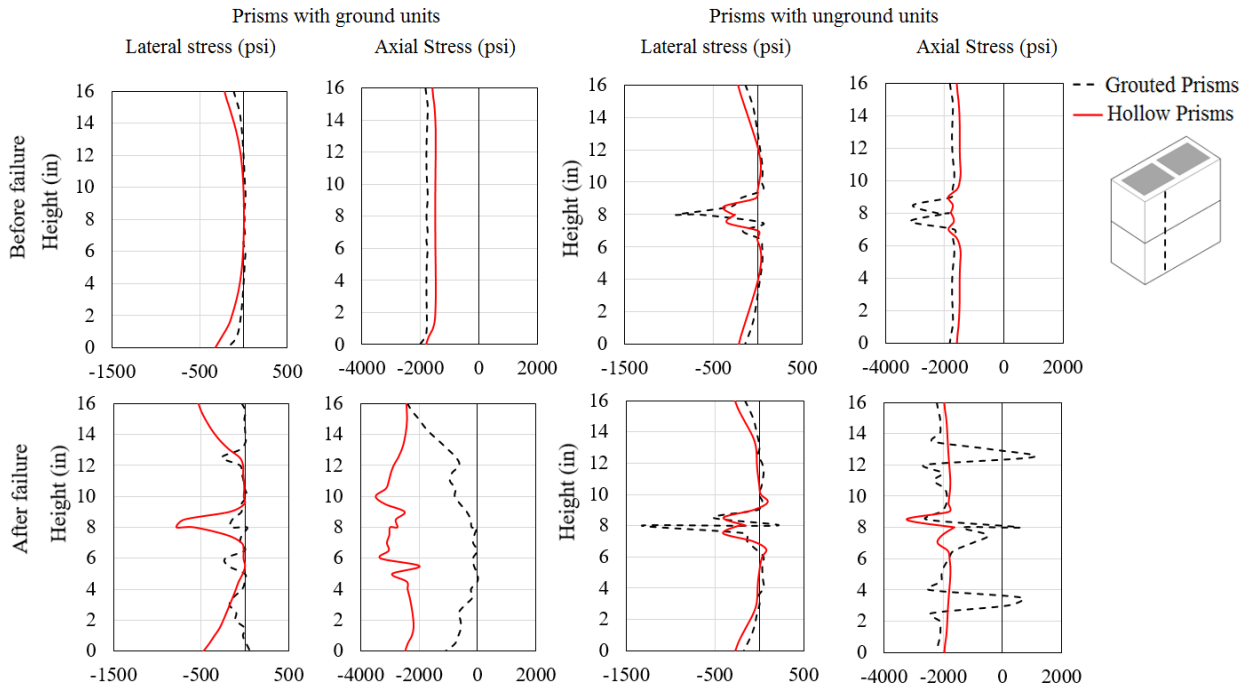

Fig. 16. Stress distribution across the height of the face shell before and after failure in the prism with ground and unground units.

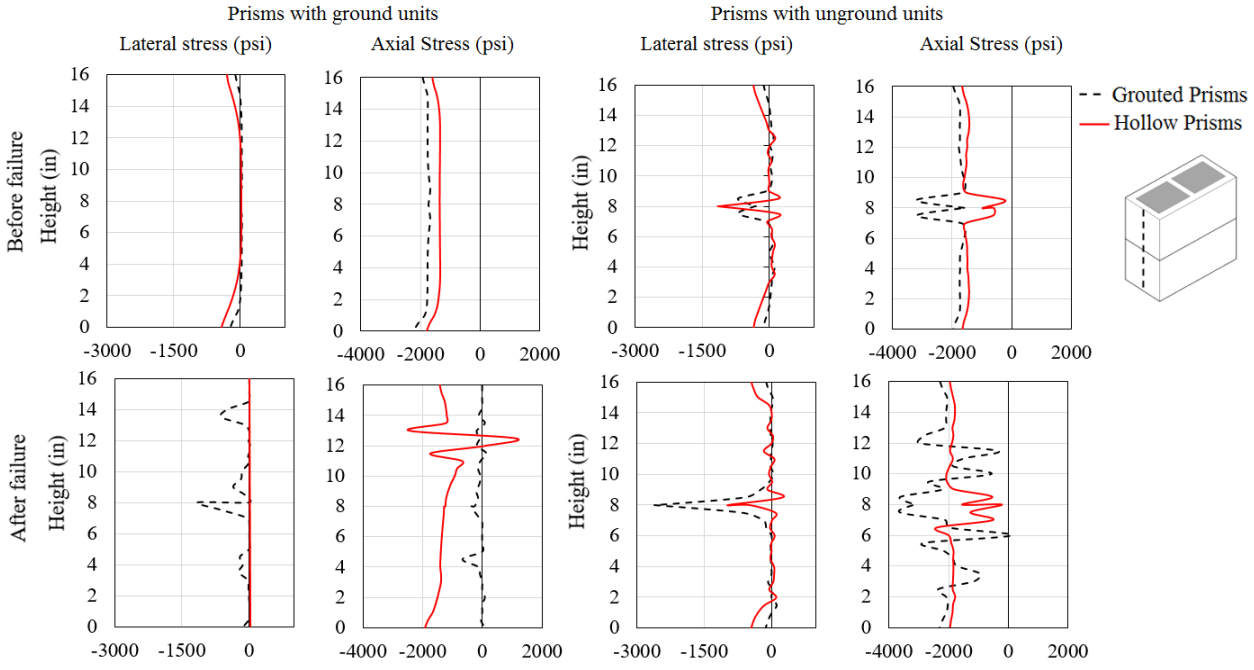

Fig. 17. Stress distribution across the height of the end shell before and after failure in the prism with ground and unground units.

Grout and the contact condition between units greatly influence the failure pattern (Fig. 18). For both hollow and grouted prisms with ground units (see Fig. 18a and Fig. 18b), cracking in the end shells is followed by cracking in the web and face shell. Prisms with unground unit surfaces demonstrate a different cracking pattern (see Fig. 18c and Fig. 18d). For both hollow and grouted prisms, stress concentration in the contact area between units is followed by cracks that appear in the following sequence: the end shell, web, and face shell.

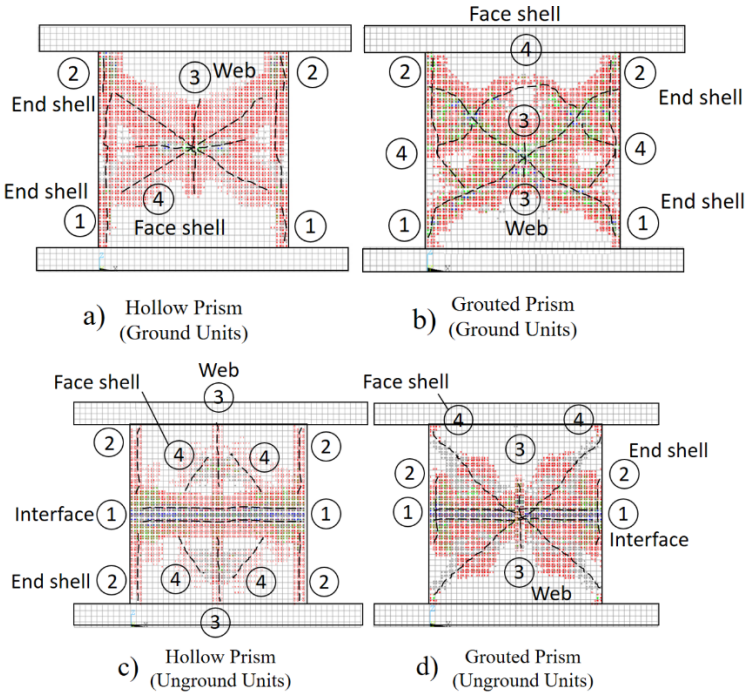

Fig. 18. Failure sequence in hollow and grouted prisms with ground and unground units (face shell view).

5. Conclusions

Numerical models provide an efficient means of predicting the structural behavior of dry-stack masonry systems under a variety of conditions without the need for an inordinate number of experiments. In this study, experimental tests on dry-stacked prisms are used to inform and assess the validity of the numerical simulation predictions. The FE models include material nonlinearity

and nonlinear boundary conditions at the contact surfaces to capture the local behavior in the models. The FE models incorporate two different levels of surface roughness at the bed joint, i.e., representing prisms with ground and unground units. These two types of prisms exhibit different behaviors under compressive loads, confirming that the surface topography influences the mechanical behavior of the prisms.

Finally, the FE models are used to predict the behavior of dry-stacked prisms by carrying out a parametric study. The main findings are:

- There is a near-linear relationship between unit strength and prism strength for both ground and unground units and all levels of surface roughness considered in this study. Prisms with unground units exhibit approximately 15% less capacity than prisms with ground units.
- The tensile strength of masonry assemblies is typically approximated as 10% of the compressive strength. Increasing this ratio in increments of 2% (i.e., to 12, 14,...20%) results in an increase in the ultimate capacity by 7-11% for prisms with ground units and 8-12% for prisms with unground units.
- Failure mechanisms of prisms with varying unit sizes are observed to be consistent. This observation holds true for prisms with both ground and unground units. For prisms with ground units, compressive stresses are observed to be uniformly distributed, whereas for prisms with unground units, compressive stresses are concentrated near the bed joint.
- For fully grouted prisms, the grout contributes to the compressive strength by a constant amount independent of the unit strength. This amount however depends on whether the units are ground or unground. The ultimate strength of fully grouted prisms with ground and unground units is observed to be nearly identical.

In future studies, the approach presented in this paper for modeling rough unit surfaces can be applied to extend the understanding of dry-stack masonry assemblies under eccentric axial, flexural, and shear loads. The modeling technique can also be used to study non-standard units (i.e., those with interlocking components). Based on the results presented herein, look-up tables can be developed and implemented in future construction codes.

Acknowledgments

The authors acknowledge the support of the National Concrete Masonry Association Education and Research Foundation for their funding of this project. They also wish to convey their appreciation to Seth Adams, Danny Metz, and Scott Black for their assistance in conducting this prism analysis and to Saurabh Prabhu, who provided insight and expertise.

References

Ainsworth, M. (2001). "Essential Boundary Conditions and Multi-point Constrains in Finite Element Analysis." *Computer Methods in Applied Mechanics and Engineering*, 190(48), 6323-6339.

Anand, K. and Ramamurthy, K. (2000). "Development and Performance Evaluation of Interlocking-Block Masonry." *J. Archit. Eng.*, 10.1061/(ASCE)1076-0431(2000)6:2(45), 45-51.

Anand, K., and Ramamurthy, K. (2005). "Development and Evaluation of Hollow Concrete Interlocking Block Masonry System." *The Masonry Society Journal*, 23(1), 11-20.

Andreev, K., Sinnema, S., Rekkik, A., Allaoui, S., Blond, E., and Gasser, A. (2012). "Compressive Behavior of Dry Joints in Refractory Ceramic Masonry." *Construction and Building Materials*, 34(1), 402-408.

ANSYS® Academic Research. Release 15.0. *Help System, Element Reference* ANSYS, Inc.

ASTM. (2010). "Standard Test Method for Young's Modulus, Tangent Modulus, and Chord Modulus." *ASTM E111-04*, West Conshohocken, PA.

ASTM. (2011). "Standard Test Method for Compressive Strength of Masonry Prism." *ASTM C1314-11a*, West Conshohocken, PA.

ASTM. (2014). "Standard Test Methods for Sampling and Testing Concrete Masonry Units." *ASTM C140/C140M-14*, West Conshohocken, PA.

ASTM. (2015). "Standard Test Method for Measuring Pavement Macrotexture Depth Using a Volumetric Technique." *ASTM E965-15*, West Conshohocken, PA.

ASTM. (2016a). "Standard Specification for Grout for Masonry." *ASTM C476-16*, West Conshohocken, PA.

ASTM. (2016b). "Standard Test Method for Sampling and Testing Grout." *ASTM C1019-16*, West Conshohocken, PA.

ASTM. (2016c). " Standard Practice for Capping Concrete Masonry Units, Related Units and Masonry Prisms for Compression Testing." ASTM C1552-16, West Conshohocken, PA.

Atamturktur, S. (2009). "Verification and Validation under Uncertainty Applied to Finite Element Models of Historic Masonry Monuments." *Proceedings of the IMAC-XXVII*, Orlando, Florida, USA. February 9-12.

Atamturktur, S., Ross, B. E., Thompson, J., and Biggs, D. (2016). "Compressive Strength of Dry-Stacked Concrete Masonry Unit Assemblies." *Journal of Materials in Civil Engineering*, 29(2), 1-4.

Baggio, C., and Trovaluski, P. (1993). "Discrete Models for Joined Block Masonry Walls." *Proc., 6th North American Masonry Conf.,* Drexel University, PA, 939-949.

Bathe, K. (1996). *Finite Element Procedures,* Prentice Hall, NJ.

Beall, C. (2000). "New Masonry Products and Materials." *Prog. Struct. Engng. and Mater.*, 2(3), 296-303.

Bertsekas, D. (1996). *Constrained Optimization and Lagrange Multiplier Methods,* Athena Scientificm, Belmont, Massachusetts.

Campbell, J. (2012). "Numerical Model for Nonlinear Analysis of Masonry Walls." *Ph.D. thesis*, Rheinisch-Westfälischen Technischen Hochschule Aachen University, Aachen, Germany.

Chen, W. (1982). *Plasticity in Reinforced Concrete,* McGraw-Hill, NY.

Contamine, R., Si-Larbi, A., Than, N. Q., and Hamelin, P. (2011). "Numerical Modeling of Reinforced Concrete Beams under Shear Stress with and without External Textile-Reinforced Concrete Reinforcement." *Journal of Reinforced Plastics and Composites*, 30(15), 1293-1303.

Cunningham, P. (2014). "Why Use MPC Based Contact for "Bonded" Connections?." *CAE Associates,* accessed 26 March, 2016, https://caeai.com/.

Dahl, K. (1992). "A Failure Criterion of for Normal and High Strength Concrete." *Rep. R. 286,* Depart. Struc. Engng, Technical Univ. of Denmark, Lyngby, Denmark.

Dahmani, L., Khennane, A., and Kaci, S. (2010). "Crack Identification in Reinforced Concrete Beams Using ANSYS Software." *Strength of Materials*, 42(2), 232-240.

Drucker, D., Prager, W., and Greenberg, H. (1952). "Extended Limit Design Theorems for Continuous Media." *Quart. Appl. Math.*, 9(4), 381-389.

Drysdale, R., Hamid, A., and Baker, L. (1994). *Masonry Structures: Behavior and Design,* Prentice-Hall, NJ.

Fanning, P. (2001). "Nonlinear Models of Reinforced and Post-tensioned Concrete Beams." *Electronic Journal of Structural Engineering*, 2(1), 111-119.

Ferozkhan, M. (2005). "Development of a Dry Stack Masonry System for Effective Resistence to Out-of-Plane Bending." *M.S. thesis,* Central Queensland University, Brisbane, Australia.

Gorst, N.J., Williamson, S.J., Pallett, P.F., and Clark, L.A. (2003). *Friction in Temporary Works,* Research Report 071, University of Birmingham, Edgbaston, Birmingham, UK.

Jaafar, M., Thanoon, W., Najm, A., Abdulkadir, M., and Ali, A. (2006). "Strength Correlation between Individual Block, Prism and Basic Wall Panel for Load Bearing Interlocking Mortarless Hollow Block Masonry." *Construction and Building Materials*, 20(7), 492-498.

Jackson, R., and Streator, J. (2006). "A Multi-scale Model for Contact between Rough Surfaces." *Wear*, 261(1), 1337-1347.

Kachlakev, D., Miller, T., Yim, S., Chansawat, K., and Potisuk, T. (2001). *Finite Element Modeling of Reinforced Concrete Structures Strengthened with FRP Laminates,* Final Report: Oregon Department of Transportation, OR.

Kaushik, H., Rai, D., and Jain, S. (2007). "Stress-Strain Characteristics of Clay Brick Masonry under Uniaxial Compression." *J. Mater. Civ. Eng.*, 10.1061/(ASCE)0899-1561(2007)19:9(728), 728-739.

Klingner, R. (2010). *Masonry Structural Design.* McGraw-Hill Education, NY.

Köksal, H. O., Karakoc, C., and Yildirim, H. (2005). "Compression Behavior and Failure Mechanisms of Concrete Masonry Prisms." *Journal of Materials in Civil Engineering*, 17(1), 107-115.

Kwasniewski, L. (2013). "Application of Grid Convergence Index in FE Computation." *Bulletin of the Polish Academy of Sciences*, 61(1), 123-128.

Laursen, T. (2003). *Computational Contact and Impact Mechanics,* Springer, NY.

Lin, K., Totoev, Y., Liu, H., and Wei, C. (2015). "Experimental Characteristics of Dry Stack Masonry under Compression and Shear Loading." *Materials*, 8(12), 8731-8744.

Lourenço, P. B., Oliveira, D. V., Roca, P., and Orduña, A. (2005). "Dry Joint Stone Masonry Walls Subjected to In-plane Combined Loading." *Journal of Structural Engineering*, 131(11), 1665-1673.

Lü, W., Wang, M., and Liu, X. (2011). "Numerical Analysis of Masonry Under Compression via Micro-Model." *Advance Materials Research* 243-249, 1360-1365.

Madenci, E., and Guven, I. (2015). *The Finite Element Method and Applications in Engineering Using ANSYS,* Springer, NY.

Mahboubi, A., and Ajorloo, A. (2005). "Experimental Study of the Mechanical Behavior of Plastic Concrete in Triaxial Compression." *Cement and Concrete Research*, 35(1), 412-419.

Marzahn, G. (1999). "Investigation on the Initial Settlement of Dry-stacked Masonry Under Compression." *Liepzig Annual Civil Engineering Report 3,* 353-365.

Michel, K. (2015). "Failure Behaviour of Masonry under Compression Based on Numerical and Analytical Modelling." *Ph.D. Dissertation*, Technische Universität Dresden, Germany.

MSJC, Masonry Standards Joint Committee. (2013). *Building Code Requirements and Specification for Masonry Structures and Related Commentaries,* TMS 602-11/ACI 530.1-11/ASCE 6-11, Boulder, CO.

Murray, E. (2007). "Dry Stacked Surface Bonded Masonry - Structural Testing and Evaluation." *M.S. thesis,* Brigham Young University, Provo, UT.

Oh, K. (1994). "Development and Investigation of Failure Mechanism of Interlocking Mortarless Block Masonry System." *Ph.D. Dissertation.* Drexel University, PA.

Parvanova, S., Kazakov, K. S., Kerelezova, I., Gospodinov, G., and Nielsen, M. P. (2005). "Modelling the Nonlinear Behaviour of R/C Beams with Moderate Shear Span and Without Stirrups using ANSYS". *Proc. of Scientific International Conference, VSU "Liuben Karavelov"*, 26-27 May, Sofia, Bulgaria

Pave, R. (2007). "Strength Evaluation of Dry-stack Masonry." *M.S. thesis,* University of the Witwatersand, Johannesburg, South Africa.

Peng, W., and Bhushan, B. (2001). "Three-dimensional Contact Analysis of Layered Elastic/Plastic Solids with Rough Surfaces." *Wear*, 249(1), 741-760.

Prabhu, S., Atamturktur, S., Brosnan, D., Messier, P., and Dorrance, R. (2014). "Foundation Settlement Analysis of Fort Sumter National Monument: Model Development and Predictive Assessment." *Engineering Structures*, 65(1), 1-12.

Ramamurthy, K., and Nambiar, K. (2004). "Accelerated Masonry Construction: Review and Future Prospects." *Progress in Structural Engineering and Materials*, 6(1), 1-9.

Roache, P.J. (1994). "Perspective: A Method for Uniform Reporting of Grid Refinement Studies." *ASME J. Fluids Eng.,* 116(3), 405-413.

Safiee, N., Jaafar, M., Noorzaie, J., and Kadir, M. (2009). "Finite Element Analysis of Mortarless Wall Panel." *Report and Opinion*, 1(2), 1-16.

Salas, C., and Sánchez, H. (2012). "Structural Behavior of Process Steel Towers Submitted to Seismic Actions." *Proc. 15th World Conference on Earthquake Engineering,* Lisbon, Portugal.

Sayed-Ahmed, E. Y., and Shrive, N. G. (1996). "Nonlinear Finite-Element Model of Hollow Masonry." *Journal of Structural Engineering*, 122(6), 683-690.

Schwer, L. (2008). "Is Your Mesh Refined Enough? Estimating Discretization Error Using GCI." *7th LS-DYNA Anwenderforum,* Bamberg, I-I-45-54.

Sellgren, U., Björklund, S. and Andersson, S. (2003). "A Finite Element-based Model of Normal Contact between Rough Surfaces." *Wear*, 254(11), 1180-1188.

Stefanou, I., Sab, K., and Heck, J. V. (2015). "Three-Dimensional Homogenization of Masonry Structures with Building Blocks of Finite Strength: A Closed Form Strength Domain." *International Journal of Solids and Structures*, 54, 258-270.

Subramani, T., Manivannan, R., and Kavitha, M. (2014). "Crack Identification in Reinfoced Concrete Beams Using Ansys Software." *Journal of Engineering Research and Applications*, 4(6), 133-141.

Thamboo, J. A., Dhanasekar, M., and Yan, C. (2013). "Flexural and Shear Bond Characteristics of Thin Layer Polymer Cement Mortared Concrete Masonry." *Construction and Building Materials*, 46(1), 104-113.

Thamboo, J. A., and Dhanasekar, M. (2015). "Characterisation of Thin Layer Polymer Cement Mortared Concrete Masonry Bond." *Construction and Building Materials*, 82, 71-80.

Thanoon, W., Jaafar, M., Noorzaei, J., Razali, M., Kadir, A., and Fares, S. (2007). "Structural Behavior of Mortar-Less Interlocking Masonry System Under Eccentric Compressive Loads." *Advances in Engineering,* 10(1), 11-24.

Truong-Hong, L., and Laefer, D.F. (2008). "Micro vs. Macro Models for Predicting Building Damage Underground Movements." *Proc. International Conference on Computational Solid Mechanics,* Hochiminh City, Viernam, 1-10.

Vasconcelos, G., and Lourenço, P. (2009). "Experimental Characterization of Stone Masonry in Shear and Compression." *Construction and Building Materials*, 23(11), 3337-3345.

William, K., and Warnke, E. (1974). "Constritutive Model for the Triaxial Behavior of Concrete." *Proc. Seminar on Concrete Structures Subjected to Triaxial Stresses,* Int. Association of Bridge and Structural Engineering, Zurich, Switzerland.

Yastrebov, V., Anciaux, G., and Molinari, J. (2012). "Contact between Representative Rough Surfaces." *Physics Review*, 86(3), 1-18.

Yastrebov, V., Anciaux, G., and Molinari, J. (2015). "From Infinitesimal to Full Contact between Rough Surfaces: Evolution of the Contact Area." *Journal of Solids and Structures*, 52(1), 83-102.

EXPERIMENTAL AND NUMERICAL EVALUATION OF REINFORCED DRY-STACKED CONCRETE MASONRY WALLS

Marcos Martínez[1] and Sez Atamturktur[2]

Abstract

In dry-stack concrete masonry systems, masonry units are laid without mortar joints, reducing the cost and increasing the speed of construction. Despite these advantages, mortarless construction is not yet widely implemented, primarily because the behavior of dry-stack masonry wall systems is not yet fully understood. To address this need, we developed experimentally validated finite element models of dry-stacked concrete masonry walls, and using these models, investigated the effect of various design parameters (e.g., unit and grout compressive strength, yield strength, and reinforcement and grouting ratios) on the out-of-plane load carrying capacity and failure modes of the walls. With the results of the parametric analysis, we then derived semi-empirical relationships that approximate the load-carrying capacity of reinforced dry-stacked concrete masonry walls. The present paper reports the findings obtained from this combined experimental and numerical study to support the development of future design guides for dry-stack systems.

Keywords: out-of-plane bending, finite element analysis, flexural behavior, mortarless masonry construction.

[1] Ph.D. Candidate, Dept. of Civil Engineering, Clemson Univ., Clemson, SC 29634
[2] Distinguished Professor, Dept. of Civil Engineering, Clemson Univ., Clemson, SC 29634 (corresponding author), E-mail: sez@clemson.edu

1. Introduction

In dry-stack concrete masonry construction, the units are laid without mortar bonding the joints. This type of masonry construction requires smaller amounts of wet material and reduces the need for highly skilled labor, thereby reducing workmanship cost (Murray 2007; Uzoegbo et al. 2007) and resulting in significantly improved efficiency (Anand and Ramamurthy 2003). Mortarless construction is, however, a low bending capacity system. Hence, the dry-stacked walls bearing lateral loads (e.g., wind, soil pressure, seismic loads, and eccentric gravity loads) need to be augmented to increase their bending capacity through the use of interlocking units, grouting, steel reinforcement, post-tensioning, surface bonding or a combination of these techniques (Glitza 1991; Lohr 1992; Marzahn 1997; Biggs 2002; Murray 2007; Biggs and Forsberg 2008; Okail et al. 2016).

Recently, several proprietary mortarless construction systems, a significant portion of which involve interlocking units, have become available on the market. The studies investigating these proprietary systems constitute the vast majority of the literature on dry-stack construction (Hatzinikolas et al. 1986; Vargas 1988; Harris et al. 1992; Hines 1993; Drysdale and Guo 1995; Anand and Ramamurthy 2000; Uzoegbo 2001; Thanoon et al. 2004; Uzoegbo and Ngowi 2004; Ferozkhan 2005; Ngowi 2005; Pave 2007; Safiee et al. 2011; Molnár and Jönsson 2012). The primary focus of the pertinent literature on the various shapes and forms of these proprietary interlocking units and the scarcity of generally applicable findings regarding the behavior of dry-stack masonry systems have contributed to the current lack of a unifying building code regulating the construction with mortarless masonry assemblies.

To help address this knowledge gap, the present study aims to obtain generalizable findings regarding the behavior of dry-stacked wall systems. For this, we focus on standard (8 in.×8 in.×16

in.) concrete masonry units (CMUs), i.e., the CMU type most commonly used in the United States (Heiserman 2015), and develop experimentally validated finite element models to overcome the need to conduct prohibitively resource-intensive experimentation. The predictive models are developed here to predict the mechanics of the structural failure and hence, to represent the ultimate behavior of the walls, major sources of nonlinear behavior are taken into account in these models, including: (1) material nonlinearity (i.e., the nonlinear characteristics of the concrete masonry units, grout and reinforcing bars) due to plasticity, cracking and crushing; (2) geometric nonlinearity due to large displacements prior to failure (i.e., P-Δ effects); and (3) contact nonlinearity due to changes in stiffness when bodies come in or out of contact with each other. To ensure that these predictive models are accurate representations of reality, experiments are conducted in the laboratory and model predictions are checked against experimental observations. These experimentally validated models are then used to investigate the ultimate behavior and failure modes of various wall designs, providing previously unavailable knowledge regarding the behavior of dry-stacked walls to aid in the development of future design codes.

2. Reinforced Dry-stacked Concrete Masonry Walls Test

To obtain experimental data regarding the flexural behavior of reinforced, grouted dry-stacked masonry walls, four nominally identical wall specimens are tested under 4-point out-of-plane loading using a self-reacting steel test frame and a hydraulic jack (Fig. 1). The wall specimens stand vertically on a frictionless ground surface and withstand lateral loads imparted by frictionless rollers at two loading and two supporting points. To prevent local crushing of the CMU at the loading locations, light-gauge steel platens are positioned between the walls and rollers. The two-line loads are applied by a hydraulic actuator, specifically the ENERPAC RCH302, bolted to the self-reacting steel frame.

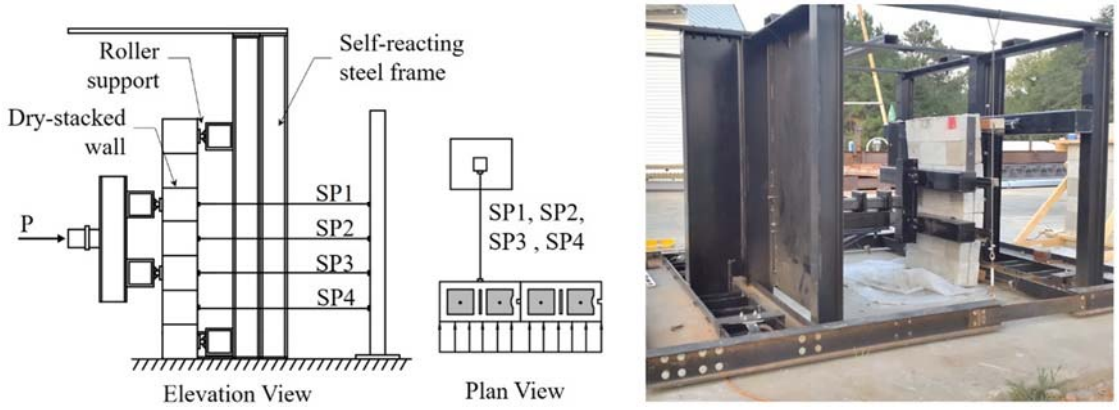

Fig. 1. Representative dry-stacked wall test setup, elevation view and plan view (left), photo taken during experiments (right).

The wall specimens are 32 in. (two units) wide by 56 in. (seven courses) high and built with nominal 8 in.×8 in.×16 in. CMUs to meet the requirements of ASTM C90 (ASTM 2016c), with half units being placed at the ends of every second course. The wall specimens are fully grouted with pre-mixed non-shrink grout prepared on site and reinforced with No. 3 reinforcing steel bars constituting 0.18% of the cross-sectional area of the wall. When the wall is fully engaged, the applied load is measured with a pressure gauge and the corresponding wall displacement is measured with string pots at four locations as shown in Fig. 1, i.e., at point line loads (SP1 and SP3), mid-height (SP2) and between the lower support and line load (SP4). The load and the displacement data recorded during the experiments and are shown in Table 1.

Table 1. Wall test results for SP locations.

Wall	Ultimate Load (k)	Ultimate Displacements (in.) SP1	SP2	SP3	SP4
W1	23.520	1.348	1.603	1.475	0.907
W2	23.021	1.595	2.238	2.026	1.289
W3	26.129	1.472	2.029	1.836	1.119
W4	24.571	1.501	2.043	1.867	1.032
Mean	24.307	1.475	1.975	1.795	1.087

3. Numerical Models for Reinforced Dry-stacked Walls

In parallel with the laboratory experiments, finite element (FE) models are developed in ANSYS v.15 to numerically simulate the behavior of the tested reinforced dry-stacked concrete masonry walls (see Fig. 2). These FE models are developed using the actual unit dimensions of a concrete masonry two-core stretcher with a 7⅝ in. depth and height, a 15⅝ in. length, a 1¼ in. thickness in the face shell and a 1 in. thickness in the end shell and web. Fillets at the inner and outer edges and the tapering of the web are excluded from the model geometry to simplify the mesh discretization.

The interfaces between the CMUs are modeled using contact elements to reflect the discontinuity (i.e., lack of bonding) between units typical in dry-stack construction. The grout in the cells is modeled monolithically along the height of the wall, and full bonding is assumed between the grout and the CMUs as well as between the grout and the reinforcing bars.

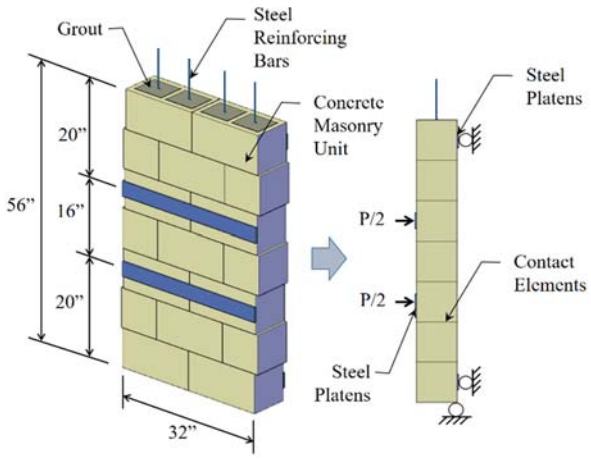

Fig. 2. Reinforced dry-stack concrete masonry wall model.

To represent the 4-point bending scenario, steel platens are modeled to uniformly distribute the load at the point of contact along the width of the wall to prevent stress concentrations. Two platens are located on one side of the wall to act as supports and to represent part of the self-reacting steel test frame discussed in Section 2. These platens are attached to the wall to allow rotations but restrain horizontal movement. On the other side of the wall, two more platens are attached to the units to distribute the line loads applied by the hydraulic jack. The frictionless boundary condition at the base of the wall is represented by restraining vertical movements but allowing rotations and lateral movement at the edge of the bottom of the wall as shown in Fig. 2.

3.1 Element Types and Material Models

Elements types and material models are selected to represent two major effects (see Fig. 3), (i) *cracking* and *crushing* in the grout and/or units and (ii) *plasticity* in the grout and/or units and in the steel reinforcing bars.

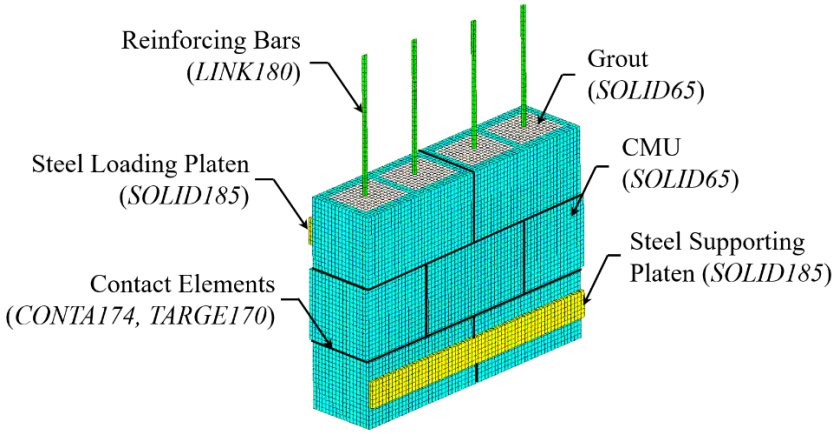

Fig. 3. Element types in the reinforced dry-stacked wall.

Concrete Masonry Units and Grout. Concrete masonry units and grout are modeled using the *SOLID65* element from the ANSYS library. *SOLID65* is an 8-noded tridimensional solid isoparametric hexahedron capable of crushing in compressive and cracking in tensile stresses. The material behavior of the units and the grout is represented under triaxial conditions based on the Drucker-Prager failure criterion (Drucker et al. 1952) in earlier stages of the loading, and based on the Willam-Warnke failure criterion (Willam and Warnke 1974) in the later stages, i.e., at the strength limit of the materials. These failure surfaces are shown schematically in Fig. 4.

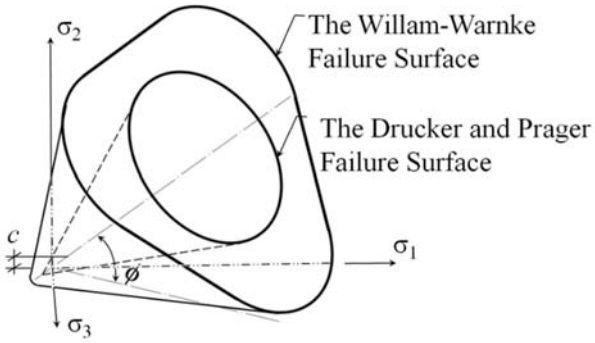

Fig. 4. Schematic failure surfaces of the units and grout material in the three orthogonal dimensions of the stress space.

The Drucker and Prager criterion introduces a perfectly plastic behavior, i.e., after the elastic limit has been reached and before crushing and cracking occurs. Widely implemented for masonry

structures (Sayed-Ahmed and Shrive 1996; Köksal et al. 2004, Angelillo et al. 2010), this criterion defines a surface formed in the principal stress space that takes into account the plastic-flow ability. This surface is characterized by two defining parameters: internal friction angle ϕ and cohesion c. In this study, for these parameters the values $\phi=36.65°-1.1°(f'_{unit}/1000)$, proposed by Dahl (1992) and Mahboubi and Ajorloo (2005), and $c=f'_{unit}/4$, proposed by Chen (1982), are used to represent the CMUs, and the values $\phi=0.01f'_{grout}$, and $c=0.129f'_{grout}+268.32$, proposed by Köksal et al. (2005), are used to represent the grout.

The Willam-Warnke criterion defines the cracking and crushing conditions of elements. Cracking occurs when the principal tensile stress in any direction lies outside its failure surface. In a cracked element, the stiffness of the finite element is set to zero in the direction parallel to the principal tensile stress orientation (Betti and Galano 2012; Prabhu et al. 2014). Crushing occurs when all principal stresses of the element are in compression and lie outside the Willam-Warnke failure surface. Both cracking and crushing are reflected by a reduction of stiffness. In this study, the stiffness of a cracked element is set to zero, while the crushed element is set at 50% of its original stiffness.

The Willam-Warnke failure surface is expressed in terms of five input parameters: the ultimate uniaxial tensile strength (f_t), the compressive strength (f'_c), the biaxial compressive strength ($f_{cb}=1.2\,f'_c$), the ultimate compressive strength for a state of biaxial compression ($f_1=1.45\,f'_c$), and an ultimate compressive strength for a state of uniaxial compression ($f_2=1.725\,f'_c$) (Kachlakev 2001).

To describe the open and closed crack behavior for concrete masonry units and grout, shear transfer coefficients for open (β_t) and closed (β_c) cracks along with a tensile crack factor (v_r) must be defined. These coefficients reflect the shear strength reduction factor for loads that induce

sliding across the crack face. Shear transfer coefficients range from values of 0 to 1, with 0 representing a smooth crack with no shear transfer and 1 a rough crack with full shear transfer. The value v_r is a multiplier that accounts for the amount of tensile stress relaxation. In the present study, β_t is set to 0.2, β_c to 0.6, and v_r to 0.6.

Reinforcing Bars. Reinforcing bars embedded in grout are most commonly represented through one-dimensional link elements that have nodes coincident with the tridimensional solid elements of the surrounding grout mesh as shown in Fig. 5 (Tavárez 2001; Ramadan et al. 2009; Kamonna 2010; Ashour 2016). This node sharing ensures displacement compatibility and a perfect bond between the grout and the steel in the FE model.

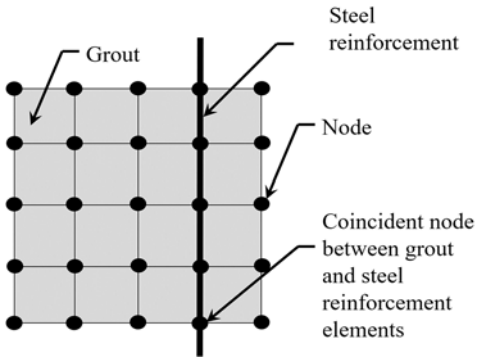

Fig. 5. Coincident nodes between SOLID65 and LINK180 elements.

In this study, steel reinforcing bars are modeled using a *LINK180* element. This element is a uniaxial spar capable of carrying an axial load and is defined by two nodes with three translational degrees of freedom at each. While this *LINK180* element does not allow bending due to its pin-jointed behavior, it allows plasticity, creep, rotation, large deflection, and large strain to be considered. A bilinear isotropic hardening plasticity model based on the Von Mises failure criteria is adopted here for the steel reinforcing bars (Asare 2015; Elmezaini and Ashour 2015). The slope of the initial portion of the stress-strain curve of the reinforcing bars is defined by the modulus of

elasticity until the yield stress is reached; then the material model is based on the tangent modulus, set to 0.01 times the modulus of elasticity.

Steel Platens. In accordance with the experiments, one-quarter inch-thick steel platens are added at the locations of the point loads and horizontal supports. These platens, modeled using 8-noded isoparametric *SOLID185* hexahedron elements, are put in place to provide an even stress distribution over the loading and supporting area. Loading and supporting lines are applied under the centerline of the steel platens to allow rotation of the platen (shown in Fig. 2).

Contact Elements. The 8-noded *CONTA174* and *TARGE170* elements are used to model the deformations and load transfer at the contact surfaces between units. As these elements have three translational degrees of freedom at each node. The contact and target elements are located on the surfaces of the three-dimensional *SOLID65* elements. In these elements, a "contact surface" and a "target surface" form a contact pair to represent sliding in the tangential direction and translation in the normal direction.

3.2 Material Property Values

Material properties (i.e., compressive strength, tensile strength and modulus of elasticity) for the CMUs, the grout and the reinforcing bars are defined as inputs for the FE model. To determine the material properties of CMUs, five individual units are tested according to ASTM C140 (ASTM 2014) using a SATEC Systems M11-400RD universal testing machine (Fig. 6). The compressive strength is determined as the average from the measurements of applied compressive force at failure and the modulus of elasticity of the CMUs as the average of the slope in the chord modulus between 5% and 33% of the unit strength according to ASTM E111 (ASTM 2010). The unit tensile strength is approximated as 10% of the compressive strength (Klingner 2010). To determine the material properties of the grout used to build the walls, five grout samples are prepared according

to ASTM C1019 (ASTM 2016b) and tested based on ASTM C39 (ASTM 2016a) to determine compressive strength and modulus of elasticity. Past studies suggest that grout tensile strength falls between 8% and 15% of its compressive strength (Wight and MacGregor 2011). Accordingly, the grout tensile strength is assumed to be 10% for this study. Material properties for the reinforcing bars are defined as specified by the manufacturer. Table 2 lists the material properties for the CMUs, the grout and the reinforcing bars.

Fig. 6. Experimental setup of the CMU test.

Table 2. Material properties by testing.

CMU	Compressive strength	2,131 ± 61 psi
	Tensile strength	213 psi
	Modulus of elasticity	2,000,000 psi
Grout	Compressive strength	5,700 ± 751 psi
	Tensile strength	570 psi
	Modulus of elasticity	1,333,333 psi
Reinforcing Bars	Designation	No. 3
	Cross section area	0.11 in^2
	Yield stress	69,000 psi
	Ultimate stress	107,000 psi
	Modulus of elasticity	29,000,000 psi

3.3 Mesh Refinement Study

Previous research has demonstrated that dry-stacked concrete masonry systems are expected to behave in a highly nonlinear fashion (De Castro 2003), the modeling of which in finite element analysis requires appropriate mesh discretization (Hemez 2005; Roache 2009). Accordingly, a mesh convergence study is conducted to determine a mesh size that yields a balance between solution accuracy and computational time, and to evaluate the numerical error due to discretization. This is important because a coarse mesh can degrade solution accuracy, while a finer mesh can result in excessive computation. The Grid Convergence Index (GCI) is a widely used estimator for the numerical uncertainty (Schwer 2008; Atamturktur 2009; Roache 2009; Kwaśniewski 2013). The GCI value is calculated as $GCI=(F_s\,\varepsilon)/(R^p-1)\times 100\%$, where F_s is a factor of safety with a suggested value of 1.25 when three mesh sizes are evaluated; ε is the difference between subsequent solutions for a group of meshes (i.e., fine (Δ_F) to medium (Δ_M) and medium (Δ_M) to course (Δ_C)) at each load stage; R denotes the refinement ratio, which is the ratio of mesh sizes; and p denotes the order of convergence.

The mid-height lateral displacement response $y(\Delta x)$ at three different load amplitudes is predicted for both linear (load level P_1) and nonlinear behavior (load levels P_2 and P_3) with three meshes ($\Delta_F=0.5$ *in.*, $\Delta_M=1$ *in.,* and $\Delta_C=2$ *in.*), where the lateral capacity is approximately 13,000 lbs. The displacement response ($y(\Delta x)$) converges from above, meaning that the numerical solutions are larger than the reference solution ($y_{reference}$). Fig. 7 shows the solution error versus the mesh size on a log-log scale, where the slope of each curve represents p. As shown in Table 3, an increase in the load results in more nonlinear behavior; the numerical uncertainty for fine-medium mesh for mid-height lateral displacement is 9.61% at load amplitude P_3. Therefore, a fine mesh of

0.5 in. provides a numerical error that remains lower than 18.83%, the maximum experimental variability for the same point of analysis.

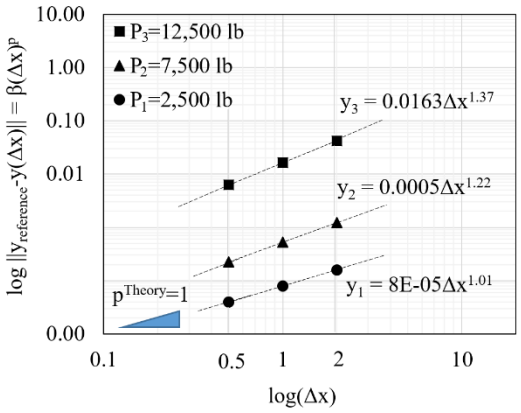

Fig. 7. Mesh refinement study showing an asymptotic convergence behavior at three load stages.

Table 3. Results of grid convergence index.

Load (lbs)	$GCI_{F\text{-}M}$ (%)	$GCI_{M\text{-}C}$ (%)	*P*	$GCI_{M\text{-}C}/R^pGCI_{F\text{-}M}$
P_3=12,500	9.61	23.21	1.37	1.20
P_2=7,500	2.88	6.57	1.22	1.14
P_1=2,500	1.38	2.74	1.01	0.98

GCI allows for the calculation of the rate of convergence to the reference solution as mesh size is reduced (i.e., as $\Delta x \rightarrow 0$). The calculated rate of convergence should ideally match the theoretical first-order convergence (i.e., $p^{theory}=1$) expected from *SOLID65* elements which have linear shape functions. Another property of the GCI is that the ratio $GCI_{M\text{-}C}/R^pGCI_{F\text{-}M}$ is expected to be close to 1 to ensure that the numerical solutions converge from above or from below.

When the rate of convergence is calculated for the three load amplitudes (P_1, P_2, and P_3) as shown in Table 3, the value of *p* is observed to be close to 1, confirming the expected behavior $\Delta x \rightarrow 0$. When the load amplitude P increases, so does the intensity of nonlinearity response of the walls, which in turn makes a finer mesh necessary. This is observed in Table 3 with increasing

deviation of the calculated p from theoretical value of 1.0. Similarly, the GCI value increases for higher load amplitudes.

4. Experimental Validation of the Numerical Models

The response of four dry-stacked masonry walls under lateral load is observed in the laboratory. These experimental observations are then compared against model predictions to assess the predictive abilities of the finite element model discussed in the previous section (see similar studies on experimental validation of masonry systems, Sekender and Page 1988; Gabor et al. 2006; Atamturktur et al. 2012a; Atamturktur et al. 2012b). Specifically, the failure pattern, the separation at the joints between the CMUs, and the load and displacement response of the walls are evaluated in this comparison.

Failure pattern. Experimentally observed and numerically predicted failure patterns are in good agreement and both reveal that dry-stacked masonry walls are likely to fail in a flexural ductile mode (Fig. 8). Cracks have a conical pattern and form first in the grout facing the tension face of the unit cell around the height of the bed joints being concentrated in the pure bending zone as shown in Fig. 9. The cracking in the grout surrounding the reinforcement reduces the bond stresses between the grout and the reinforcing steel bars. The experiments and the numerical model predictions agree on the conical failure pattern of the grout around the joints.

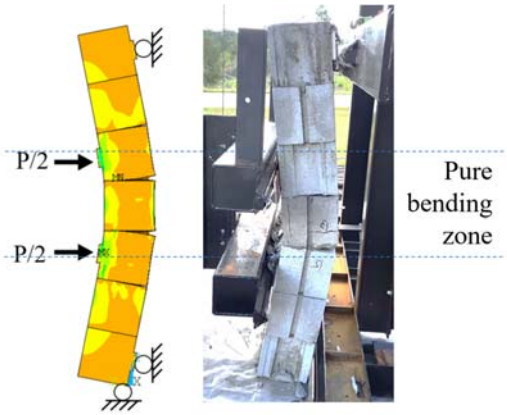

Fig. 8. Failure pattern comparison at ultimate between numerical model (left) and experiments (right).

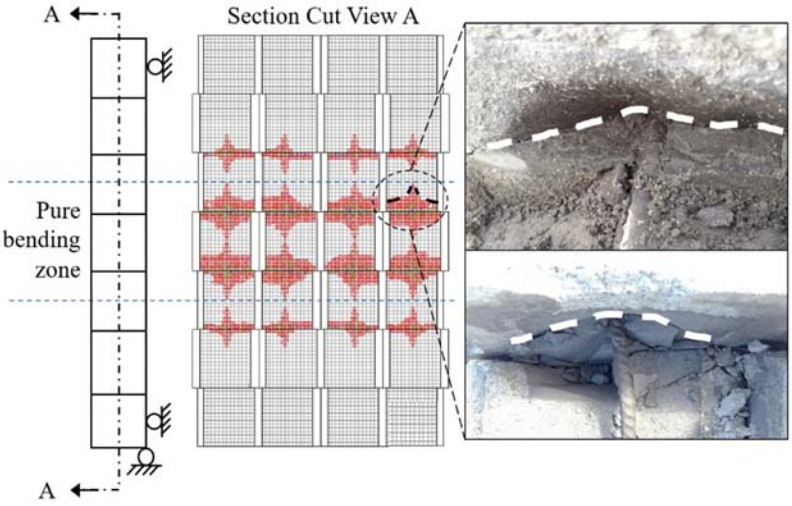

Fig. 9. Visual comparison regarding the failure pattern of the grout in the numerical model (left) and the experiments (right) at ultimate.

The model predictions also agree with the experimental observations in the failure pattern of the units in the tension face of the wall as shown in Fig. 10. The cracks in the tension face within the pure bending zone extend along the grout depth toward the compression face, causing crushing in the joints between the CMUs. The location and size of the crushed regions observed during the experiments agree with the model predictions.

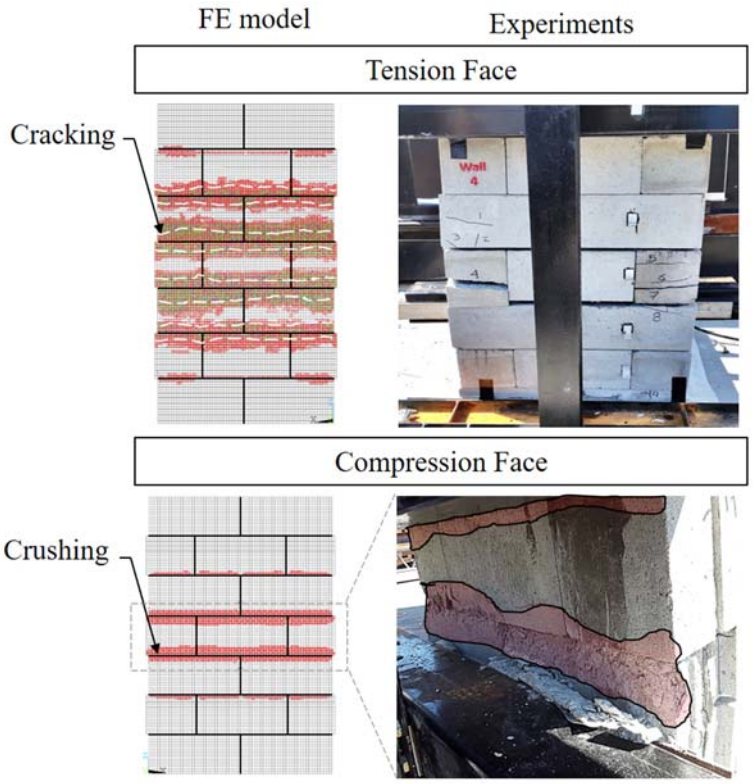

Fig. 10. Cracking in the tension face and crushing in the compression face of the units in the FE model (left) and experiments (right) at ultimate.

Separation at the bed joints. At the ultimate load, separations between the CMUs at the bed joints are manually measured with a caliper at several locations on the walls, as shown in Fig. 11. Specifically, the extent of the separations is measured on the tension face at the pure bending zone (O21-O23 and 031-O33), outside the pure bending zone (O11-O13 and O41-43), and at the contact point with the ground on the compression face (O51-O53). The minimum and the maximum separations from the measurements of the four walls tested at each location are listed in Table 4 for both the experiments and the FE model at ultimate stage.

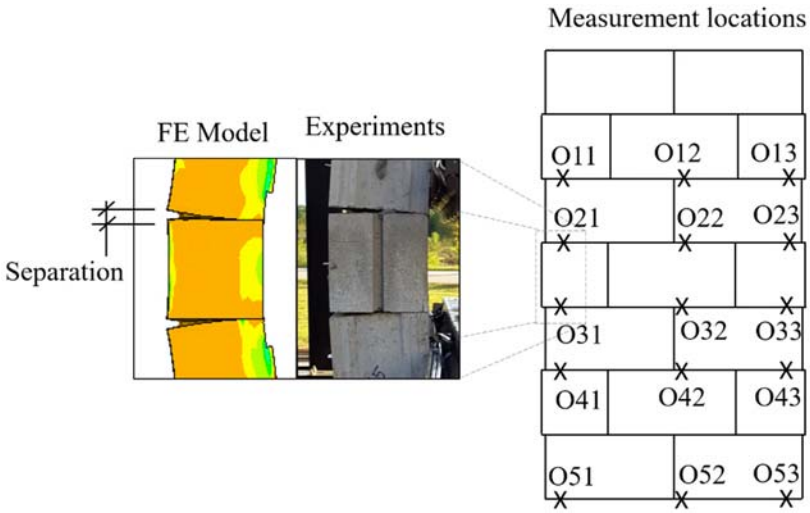

Fig. 11. Location of separation measurements at the bed joints.

Table 4. Results of separation measurements at the bed joint at ultimate.

Location	Measurements		FE Model (in.)	Within range?
	Min. (in.)	Max. (in.)		
O11	0.039	0.191	0.159	Yes
O12	0.131	0.257	0.176	Yes
O13	0.117	0.170	0.158	Yes
O21	0.394	0.628	0.462	Yes
O22	0.310	0.579	0.472	Yes
O23	0.308	0.516	0.466	Yes
O31	0.319	0.653	0.464	Yes
O32	0.202	0.961	0.474	Yes
O33	0.421	0.803	0.464	Yes
O41	0.039	0.325	0.159	Yes
O42	0.202	0.314	0.178	No
O43	0.180	0.422	0.162	No
O51	0.813	1.219	1.319	No
O52	0.825	1.219	1.329	No
O53	0.720	1.215	1.318	No

The results show that the separations predicted by the model are within the range of experimental variability, except for the lower points on the wall. The separation observed in the lower region is underestimated by the model predictions by about 10%. This discrepancy could be

explained by the fact that even though the experimental test presented a non-frictional surface on the ground, some residual friction forces appear in the contact of the wall and the ground.

Load-displacement wall response. As shown in Fig. 12, numerically and experimentally obtained load-displacement curves at different locations along the height (SP1-SP4 as discussed in Section 2) are in good agreement. The ultimate load and displacement values are compared in Table 5.

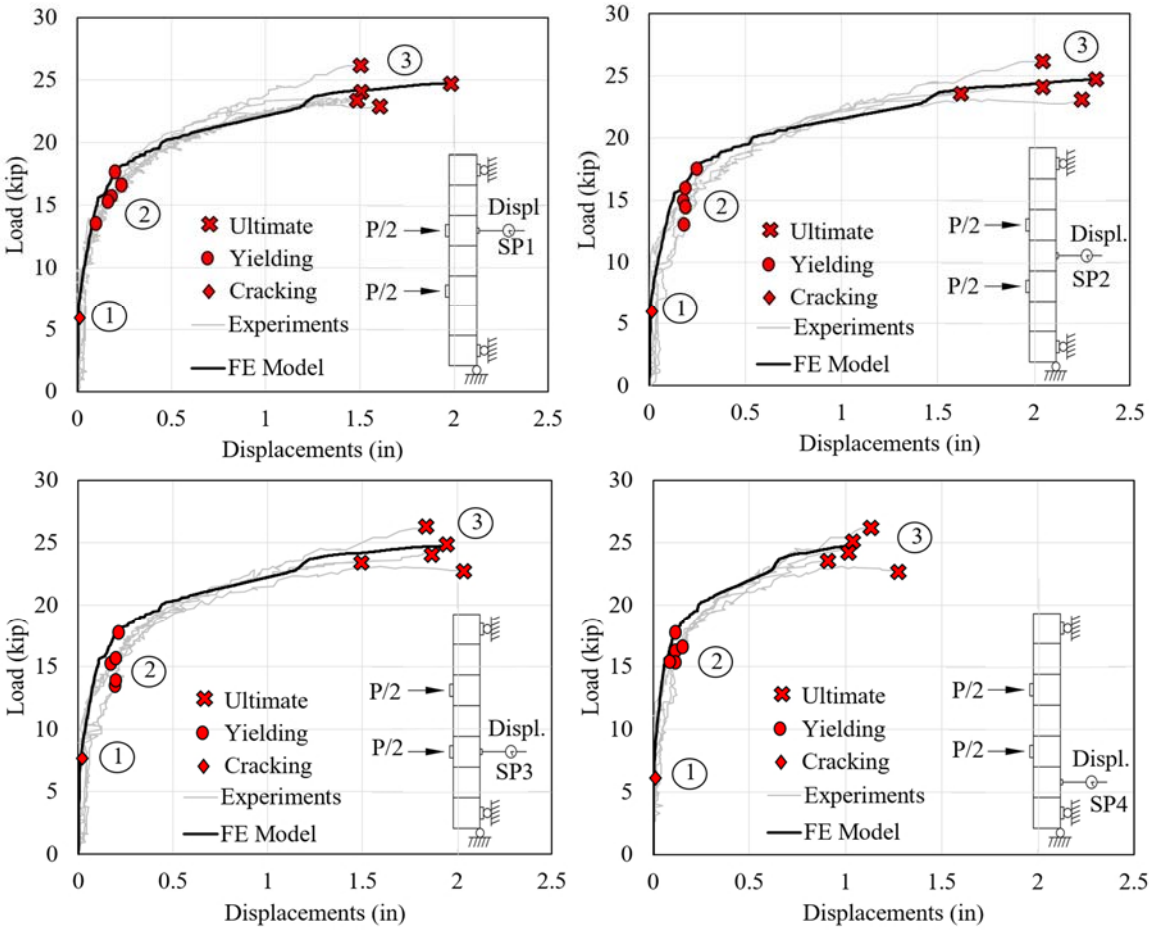

Fig. 12. Load-displacement behavior of experimental tests compared to FE model.

Table 5. Ultimate load and displacement comparison.

Response	Measurements		FE	Within
	Min	Max.	Model	range?
Disp. @ SP1 (in.)	1.340	1.590	1.971	No
Disp. @ SP2 (in.)	1.603	2.240	2.382	No
Disp. @ SP3 (in.)	1.470	2.020	1.901	Yes
Disp. @ SP4 (in.)	0.910	1.290	1.024	Yes
Ult. Load (kip)	23.020	26.120	24.731	Yes

The load-displacement behavior of the walls can be categorized in three significant stages. The first significant point in the load-deflection curve is the initiation of the cracking, indicated by the change in the slope of the initial tangent stiffness (indicated with a rhombus in Fig. 12). The second significant point in this curve is the yield point of the reinforcing bars (indicated with circles in Fig. 12). In the load-displacement curve predicted by the FE model, this transition point can be found by tracking the stresses in the steel reinforcing bars as the lateral load increases. In the load-displacement curve measured during the experiments, this point is harder to identify. Based on equivalent elasto-plastic yield approximation, Park (1988) proposed a method for identifying the displacement at the point of yielding as the intersection of the initial tangent stiffness and the tangent of the ultimate load (see Fig. 13). The third significant point in the load-displacement curve is the ultimate load capacity of the wall (indicated with crosses in Fig. 12).

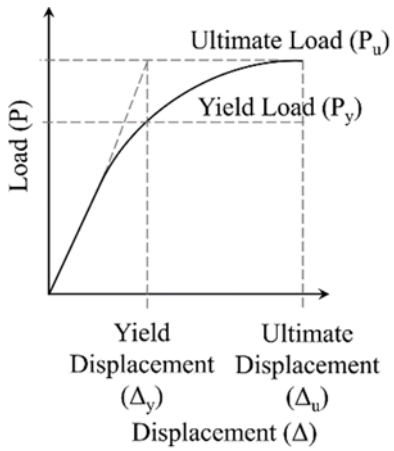

Fig. 13. Yield displacement based on equivalent elasto-plastic yield.

The reinforced dry-stacked concrete masonry walls can withstand lateral loads beyond the full elastic response as they exhibit displacement ductility. The displacement ductility (μ) can be calculated as the ratio between ultimate displacement (at Point 3 in Fig. 12) and yield displacement (at Point 2 in Fig. 12). Calculations for the displacement ductility from the four walls tested show a minimum value of 5.81 and a maximum value of 15.26; the predicted displacement ductility is 8.39. Thus, the ductility and failure response of the four walls tested and the FE model simulations are in good agreement.

5. Parametric Study of Reinforced Dry-stacked Walls

The test-analysis comparison discussed in Section 4 demonstrates that the material modeling scheme can predict the behavior of the dry-stacked walls with an acceptable agreement with the experimental observations. Accordingly, the model is used to conduct a parametric analysis investigating the influence of wall properties on the performance of dry-stack wall construction. The underlying assumption of this analysis is that the fundamental mechanistic behavior of the walls remains unchanged for varying wall properties (Atamturktur and Laman 2012; Atamturktur et al. 2012b, Van Buren et al. 2014). A parametric analysis is conducted varying one property at a time within practically plausible ranges while all other properties are kept at predefined values. The properties under study are the unit compressive strength (nominal value: 3,000 psi), the grout compressive strength (nominal value: 5,000 psi), the yield strength of the reinforcing bars (nominal value: 60,000 psi), the reinforcement ratio (nominal value: 0.18%), and the percentage of grouting (nominal value: 100%).

5.1 Effect of the Unit Compressive Strength

FE models are developed for predicting the response of fully grouted walls with varying unit compressive strengths (f_{unit}) of 2000, 3000, and 4000 psi, keeping all other properties at their

nominal values. As shown in Fig. 14, the lateral load (left) and the displacement (right) at the yield and the ultimate stages are approximated to have a linear relationship with the unit compressive strength. As the unit compressive strength increases from 2,000 to 4,000 psi, the yield load increases by approximately 2,200 lbs due to the reduction of the moment of inertia leading to the increase of the lever arm to increase the section capacity. A similar behavior for increasing unit compressive strength is also reflected in the ultimate load, which increases by approximately 6,400 lbs due to the reduction of neutral axis depth and the inelastic behavior of the compression zone. The increase in the unit compressive strength has a minimal effect in the yield displacements to remain nearly constant at approximately 0.25 in due to the steel bars reach the yield strain independently of the unit strength, while the ultimate displacements increase approximately 0.60 in. As a result, the displacement ductility ratio increases from 2 to 6.

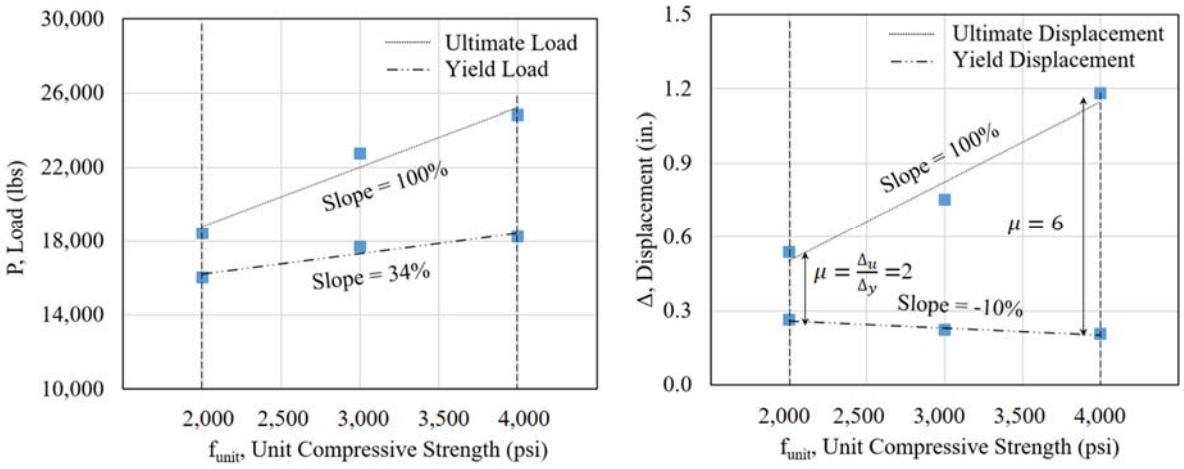

Fig. 14. Effect of unit compressive strength on the load for $2000 < f'_{unit} < 4000$: $P_u=3.20f_{unit}+12{,}390$, with $R^2=0.96$, and $P_y=1.11f_{unit}+14{,}006$, with $R^2=0.91$ (left); and displacements $\Delta_u=3E\text{-}4f_{unit}+0.14$, with $R^2=0.96$, and $\Delta_y=-3E\text{-}5f_{unit}+0.32$, with $R^2=0.94$ (right).

5.2 Effect of the Grout Compressive Strength

In addition, a parametric analysis is conducted to investigate the effect of grout compressive strength (f_{gr}) varying from 4,000 to 7,000 psi in increments of 500 psi. Similar to the preceding simulations, the remaining properties are kept constant at their nominal values. Fig. 15 are to be approximated to a linear relationship between the grout compressive strength and the lateral load (left) and the displacements (right) at the yield and the ultimate stages.

When the grout compressive strength increases from 4,000 to 7,000 psi, the behavior is similar to the variations in the unit strength. The yield load increases by approximately 2,700 lbs by the fact that a reduction of the moment of inertia leads to the increase of the lever arm to improve the section capacity. With the same increase in grout compressive strength, the ultimate load increases by approximately 4,500 lbs; the lever arm increases, leading to an inelastic behavior of the compression zone within the section. Similar to the behavior of the unit strength, the increase in the grout compressive strength causes the yield displacements remain nearly constant at 0.21 in. by the fact that the yield displacements are independent of the grout compressive strength. The ultimate displacements increase by approximately 0.5 in. due to the loss of moment of inertia in the section. This behavior causes the displacement ductility ratio to increase from 3 to 5.

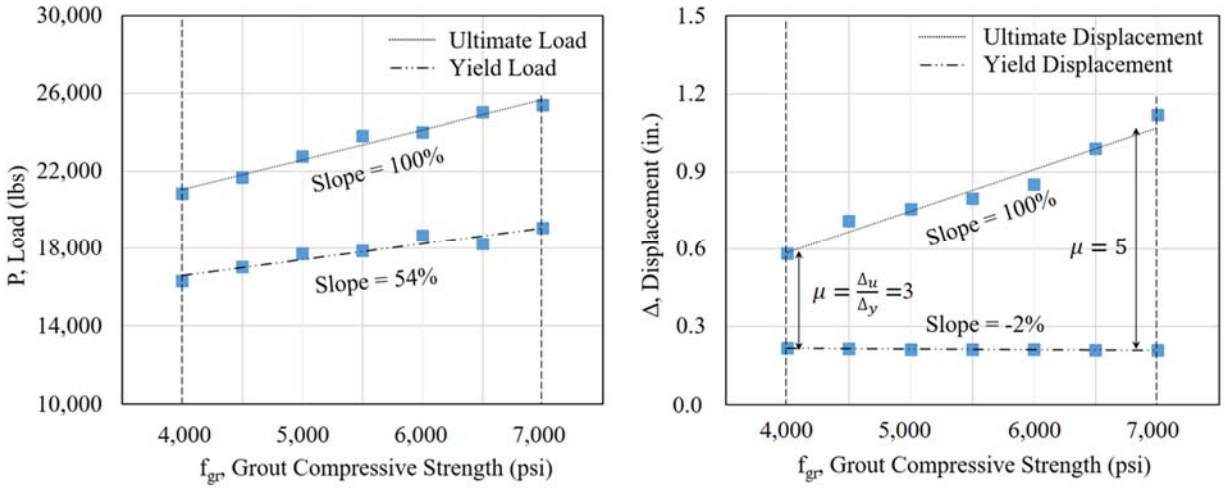

Fig. 15. Effect of grout compressive strength on the load for 4000 < f'$_{grout}$ < 7000: $P_u=1.53f_{gr}+14{,}913$, with R^2=0.97, and $P_y=0.82f_{gr}+13{,}287$, with R^2=0.90 (left); and displacements $\Delta_u=1.6E\text{-}4f_{gr}+0.06$, with R^2=0.95, and $\Delta_y=\text{-}3E\text{-}6f_{gr}+0.22$, with R^2=0.97 (right).

5.3 Effect of the Yield Strength of the Steel Reinforcing Bars

Next, the models for predicting the effect of varying the yield strength (f_y) of the steel reinforcing bars at 40,000, 60,000, 70,000, and 80,000 psi where the strain at yield of the reinforcing bar is varied accordingly are simulated. Fig. 16 are approximate to have a linear relationship between the yield strength of the steel reinforcing bars and the lateral load (left) and the displacements (right) at the yield and the ultimate stages. As the yield strength of the steel reinforcing bars increases from 40,000 to 80,000 psi, the yield load increases by approximately 7,000 lbs due to an increase in the neutral axis depth that requires a higher tension force to yield the reinforcing bars. The ultimate load remains nearly constant due to the fact that the failure is controlled by reaching the maximum useable compression strain in the extreme compression fiber in the unit. For the same increase in the yield strength of the steel reinforcing bars, the yield displacements increase by approximately 0.25 in. due to the existence of cracks, while the ultimate

displacements remain nearly constant at 0.75 in. Therefore, the displacement ductility ratio decreases from 6 to 2.

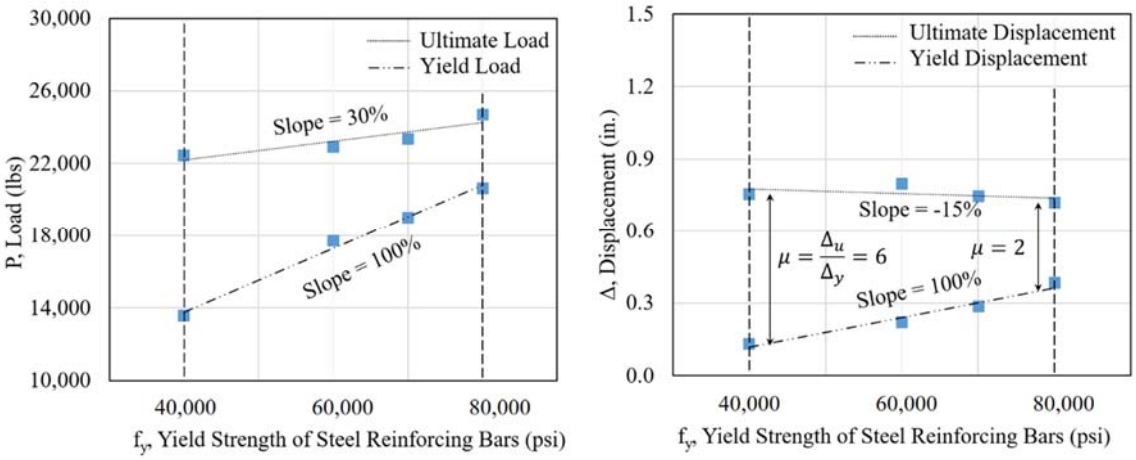

Fig. 16. Effect of yield strength of the steel reinforcement on the load for $40000 < f_y < 80000$: $P_u=0.05f_y+20{,}171$, with $R^2=0.82$, and $P_y=0.18f_y+6{,}709$, with $R^2=0.99$ (left); and displacements $\Delta_u=-9E\text{-}7f_y+0.81$, with $R^2=0.67$, and $\Delta_y=6E\text{-}6f_y\text{-}0.13$, with $R^2=0.96$ (right).

5.4 Effect of the Reinforcement Ratio

The reinforcement ratio (ρ) is studied at values of 0.0018 (0.18%) and 0.0031 (0.31%), which correspond to steel reinforcement No. 3 and No. 4 in each cell. Fig. 17 shows the relationship between the reinforcement ratio and the lateral load (left) and the displacements (right) at the yield and the ultimate stages. As the reinforcement ratio increases from 0.0018 to 0.0031, the yield load increases by approximately 5,100 lbs due to a higher tension force is required to yield the reinforcing bars. The same increase in reinforcement ratio, the ultimate load increases by approximately 2,300 lbs due to an increase in the neutral axis depth, that makes a larger compressive area in the section. The same increase in the reinforcement ratio causes the yield displacements increase by 0.12 in. due to the reduction of moment of inertia when the yielding occurs. For the ultimate displacements, there is a decrease of post-yield displacements by approximately 0.18 in. due to the behavior of the section is controlled by the compression in the

concrete. Consequently, the wall exhibits a decrease in the displacement ductility from ratio 4 to 2.

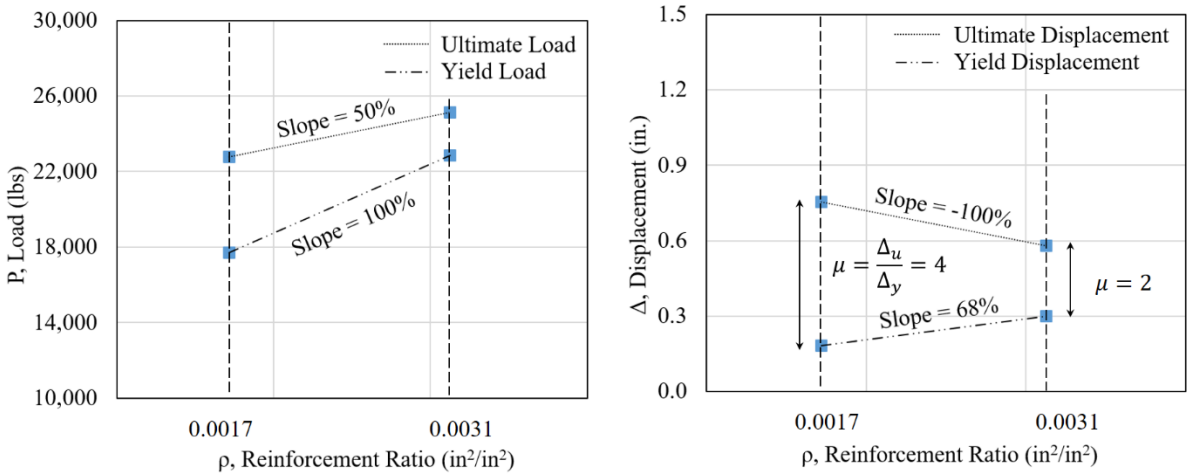

Fig. 17. Effect of reinforcement ratio for $0.0017 < \rho < 0.0031$: on the yield and ultimate loads (left); and yield and ultimate displacements (right).

5.5 Effect of the Percentage of Grouting

The effect of the percentage of grouted cells (PG) is also evaluated considering walls that are fully grouted (grout in al cells, 1.0) and those that are only partially grouted (grouted in only one cell of the unit, 0.5). The percentage of grouting is inherently linked to the reinforcement ratio, which is set to 0.0018 (0.18%) for the fully grouted wall and 0.0011 (0.11%) for the partially grouted wall. Fig. 18 shows the percentage of grouting and the lateral load (left) and displacements (right) at the yield and ultimate and yield stages. As the percentage of grouting increases from 50% (0.5) to 100% (1.0), the yield load and the ultimate loads increase by 4,700 lbs and 5,900 lbs, respectively, due to an increase reinforcement ratio. The ultimate loads increase by approximately 5,900 lbs due to an increase in cracking in the units and grout reduces the moment of inertia in the section, the neutral axis depth and the difference in the reinforcement ratio. The same increase in the percentage of grouting causes the yield displacements remain nearly constant at 0.18 in. The

ultimate displacements increase by 0.15 in. due to the fact that fully grouted walls have reduced compressive area in the section, which makes the reinforcing bars to have plastic deformations . As a result, the displacement ductility ratio has only a slight increase from 3 to 4.

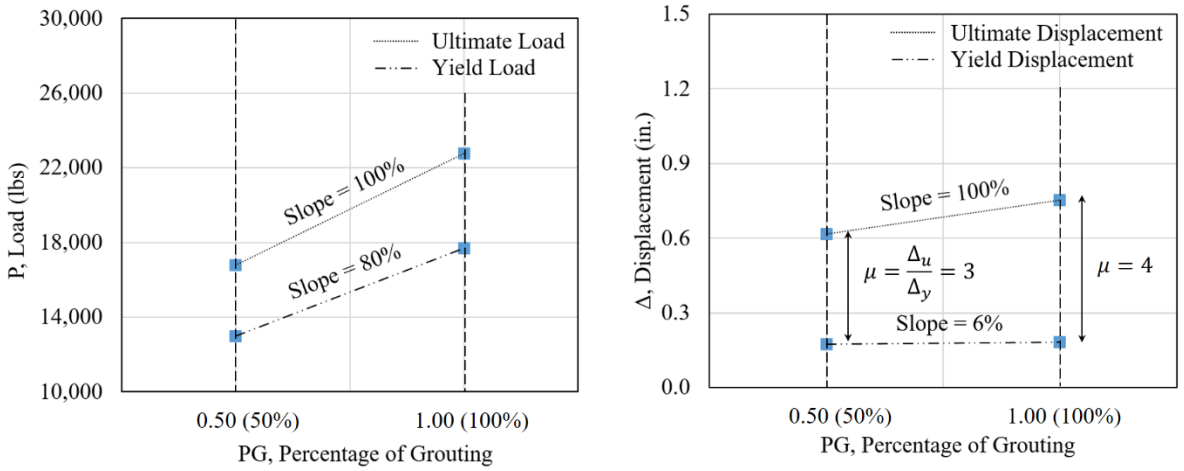

Fig. 18. Effect of percentage grouting for 0.5 < PG < 1.0: on the yield and ultimate loads(left); and yield and ultimate displacements (right).

In all, a total of 378 predictions are obtained after running all of the simulations with the varying parameters (i.e., unit and grout compressive strength, yield strength of the reinforcing bars, reinforcement ratio, and percentage of grouting). Based on the model predictions, a multivariate linear regression analysis is completed using the least squares approach to model the predictive relationships of multiple related responses on a set of independent variables; specifically, equation (1) below is proposed to predict the response of the reinforced dry-stacked concrete masonry walls. The parameter f_{unit} can take values from 2,000 to 4,000 psi, f_{gr} from 4,000 to 7,000 psi, f_y from 40,000 to 80,000 psi, ρ from 0.0018 to 0.0031, and PG either 0.5 or 1.

$$y = \beta_0+\beta_1(f_{unit})+\beta_2(f_{gr})+\beta_3(f_y)+\beta_4(\rho)+\beta_5(PG) \qquad (1)$$

The predicted response *y* and *β* coefficients are presented in the equation 2, 3, 4 and 5.

$$P_u = -1{,}233+2.55(f_{unit})+0.99(f_{gr})+585{,}601(\rho)+11{,}880(PG),\ R^2=0.89 \qquad (2)$$

$$P_y = -10{,}710+1.47(f_{unit})+0.69(f_{gr})+0.13(f_y)+2{,}403{,}833(\rho)+8336(PG),\ R^2=0.92 \quad (3)$$

$$\Delta_u = 3.9E\text{-}3\text{-}1.2E\text{-}4(f_{unit})\text{-}1.1E\text{-}4(f_{gr})\text{-}4.7E\text{-}6(f_y)\text{-}83.25(\rho)+0.28(PG),\ R^2=0.83 \quad (4)$$

$$\Delta_y = -9.67E\text{-}2+4.81E\text{-}6(f_y)+24.33(\rho),\ R^2=0.85 \quad (5)$$

6. Conclusions

Our lack of knowledge of the behavior of mortarless concrete masonry walls contributes to their limited use even though they offer time and cost advantages. This research addresses this need for information using experimental tests together with numerical models, thereby providing additional insights into the behavior of the wall and its failure. More specifically, these results describe the behavior of mortarless reinforced concrete masonry walls subjected to a 4-point bending test.

In this study, the behavior of reinforced dry-stacked walls is analyzed by observing three points of interest in the load-displacement curve, the first being the initial cracking. This point is detectable in the load-displacement curve by a reduction in the initial stiffness when the initial cracking occurs. The second significant point of interest is when the steel reinforcing bars reach the yield point, which defines the load at which the wall will experience irreversible and plastic deformations. At this point, the tension faces of the units are already cracked in the pure bending zone. Finally, the third significant point of interest is the ultimate load. Spalling in the face shells on the compression face of the units is observed, leading to crushing in the dry unit joints due to a high stress concentration. A comparison of the load-displacement curves at different locations between the FE model and the experimental test shows good agreement, supporting that the proposed FE model captures the behavior and the failure, which occurs as a hinge-like rotation along a bed joint in the pure bending zone of the reinforced dry-stacked wall.

Furthermore, this research correlates the load and displacement at the yield and the ultimate responses with variations in the unit compressive strength, grout compressive strength, yield strength of the steel reinforcing bars, the reinforcement ratio, and the percentage of grouting to determine their influence on the wall behavior. Based on the parametric study, the following conclusions can be drawn:

- An increase in the unit and the grout compressive strength improves the lateral load capacity and increases the ductility of the wall.
- When the yield strength of the steel reinforcing bars increases, the section capacity also increases, but the section ductility decreases.
- When the reinforcement ratio increases, it is clear that causes an increase in the capacity of the section; however, the higher reinforcement ratios also cause a less ductile behavior for the section.
- A change from partially to fully grouted walls leads to an improvement in the lateral load capacity of the wall and slightly increases the ductility.

The impact of these findings enriches the knowledge and the implementation of this construction system as an alternative to masonry construction. The systems have the competence to be incorporated in construction codes due to the demonstrated ability of reinforced dry-stacked walls to thrust lateral loads and exhibit a ductile mode of behavior characterized by the yielding of the steel reinforcing bars. To extend this research, in future studies, the numerical model presented in this paper can be applied to dry-stack masonry structures comprised of bonding agents, different unit geometries, and various combinations of loads to further our knowledge of these structures.

Acknowledgments

The authors acknowledge the support of the National Concrete Masonry Association Education and Research Foundation for its funding of this project. They also wish to express their appreciation to Ahmad Tarawneh, Danny Metz, and Scott Black for their assistance during the testing.

References

Anand, K.B. and Ramamurthy, K. (2000). "Development and Performance Evaluation of Interlocking-Block Masonry." *Journal of Architectural Engineering ASCE*, 6(2), 45-51.

Anand, K.B. and Ramamurthy, K. (2003). "Laboratory-Based Productivity Study on Alternative Masonry Systems." *Journal of Construction Engineering and Management ASCE*, 129(3), 237-424.

Angellillo, M, Cardamone, L., and Fortunato, A. (2010). "A Numerical Model for Masonry-Like Structures." *J. Mech. Mat. Struct.*, 5(4), 583-615.

Asare, A.K. (2015). "Finite Element Assessment of Precast Concrete Slab Using Ansys Structural." *M.S. thesis*, University of Ghana, Ghana.

Ashour, M.H. (2016). "Nonlinear Finite Element Analysis of RC Beams Strengthened with Steel Fiber-Reinforced Concrete Overlays." *Ph.D thesis*, The Islamic University of Gaza, Gaza.

ASTM. (2010). "Standard Test Method for Young's Modulus, Tangent Modulus, and Chord Modulus." *ASTM E111-04*, West Conshohocken, PA.

ASTM. (2014). "Standard Test Methods for Sampling and Testing Concrete Masonry Units." *ASTM C140/C140M-14*, West Conshohocken, PA.

ASTM. (2016a). "Standard Test Method for Compressive Strength of Cylindrical Concrete Specimens." *ASTM C39-16*, West Conshohocken, PA.

ASTM. (2016b). "Standard Test Method for Sampling and Testing Grout." *ASTM C1019-16*, West Conshohocken, PA.

ASTM. (2016c). "Standard Specification for Loadbearing Concrete Masonry Units." *ASTM C90-16*, West Conshohocken, PA.

Atamturktur, S. (2009). "Verification and Validation under Uncertainty Applied to Finite Element Models of Historic Masonry Monuments." *Proceedings of the IMAC-XXVII*, Orlando, Florida, USA. February 9-12.

Atamturktur, S., and Laman, J. (2012). "Finite Element Model Correlation and Calibration of Historic Masonry Monuments: Review." *Struct. Design Tall Spec. Build*, 21(1), 96-113.

Atamturktur, S., Li, T., Ramage, M., and Farajpour, I. (2012a). "Load Carrying Capacity Assessment of a Scaled Masonry Dome: Simulations Validated with Non-Destructive and Destructive Measurements." *Construction and Building Materials*, 34(1), 418-429.

Atamturktur, S., Hemez, F., and Laman, J. (2012b). "Uncertainty Quantification in Model Verification and Validation as Applied to Large Scale Historic Masonry Monuments." *Engineering Structures*, 43(1), 221-234.

Betti, M., and Galano, L. (2012). "Seismic Analysis of Historic Masonry Buildings: The Vicarious Palace in Pescia." *Buildings*, 2(1), 63-82.

Biggs, D.T. (2002). "Development of a Mortarless Post-Tensioned Masonry Wall System." *Proceedings of the Sixth International Masonry Conference*, 28-32.

Biggs D.T., and Forsberg, T.E. (2008). “A Mortarless Prestressed Masonry House: Case Study.” *Proceedings of the 14th International Brick and Block Masonry conference,* Sydney, Australia, 1-11.

Chen, W. (1982). *Plasticity in Reinforced Concrete,* McGraw-Hill, NY.

Dahl, K. (1992). “A Failure Criterion of for Normal and High Strength Concrete.” *Rep. R. 286,* Depart. Struc. Engng, Technical Univ. of Denmark, Lyngby, Denmark.

De Castro, D.V. (2003). “Experimental and Numerical Analysis of Blocky Masonry Structures Under Cyclic Loading.” *Ph.D. thesis*, University do Minho, Portugal.

Drucker, D., Prager, W., and Greenberg, H. (1952). "Extended Limit Design Theorems for Continuous Media." *Quart. Appl. Math.*, 9(4), 381-389.

Drysdale, R.G., and Guo, P. (1995). “Strength Characteristics of Interlocking Dry-Stacked Concrete Block Masonry.” *Seventh Canadian Masonry Symposium*, Hamilton, Ontario, 160-171.

Elmezaini, N., and Ashour, M. (2015). “Nonlinear Analysis of Concrete Beams Strengthened with Steel Fiber-Reinforced Concrete Layer.” *J. Eng. Res. Tech.*, 2(3), 181-188.

Ferozkhan, M. (2005). “Development of a Dry-Stack Masonry System for Effective Resistance to Out-of-Plane Bending.” *M.S. thesis*, Central Queensland University, Australia.

Gabor, A., Ferrier, E., Jacquelin, E., and Hamelin, P. (2006). “Analysis and Modelling of the In-Plane Shear Behavior of Hollow Brick Masonry Panels.” *Construction and Building Materials*, 20(1), 308-321.

Glitza, H. (1991). “State-of-the-Art and Tendency of Development of Masonry without Mortar.” *Proceedings of the 9th International Brock/Block Masonry Conference in Berlin*, 2, 1028-1033.

Harris, H.G., Oh, K., and Hamid, A.A. (1992). “Development of New Interlocking and Mortarless Block Masonry Units for Efficient Building Systems.” *Proceedings of the 6th Canadian Masonry Symposium, Saskatoon,* 723-734.

Hatzinikolas, M., Elwi, A. E. and Lee, R. (1986). "Structural Behavior of an Interlocking Masonry Block." *4th Canadian Masonry Symposium*, Dept. of Civil Engineering, University of New Brunswick, Fredericton, Canada, 225-239.

Heiserman, D.L. (2015). “Concrete Masonry.” *Building Construction and Finishing*. Accessed 10 30, 2016. <http://free-ed.net/free-ed/Resources/Trades/carpentry/Building01/?iNum=0702>

Hemez, F.M. (2005). “Non-linear Error Ansatz Models for Solution Verification in Computational Physics.” *Technical Report*, Los Alamos National Laboratory, Los Alamos, New Mexico. LA-UR-05-8228.

Hines, T. (1993). “Benefits of Drystack Interlocking Concrete Masonry as a Component of Cost Effective Construction.” *Proceedings of the Sixth North American Masonry Conference*, Philadelphia, PA.

Kachlakev, D.I., Miller, T., Yim, S., Chansawat, K., and Potisuk, T. (2001). *Finite Element Modeling of Reinforced Concrete Structures Strengthened with FRP Laminates*, Final Report SPR 316, California Polytechnic State University, San Luis Obispo, CA and Oregon State University, Corvallis, OR for Oregon Department of Transportation.

Kamonna, H.H. (2010). “Nonlinear Analysis of Steel Fiber Reinforced Concrete Deep Beams by ANSYS.” *Kufa Journal of Engineering*, 2(1), 109-124.

Klingner, R. (2010). *Masonry Structural Design.* McGraw-Hill Education, NY.

Köksal, H.O., Doran, B., Ozsoy, A.E., and Alacali, S., N. (2004). “Nonlinear Modeling of Concentrically Loaded Reinforced Blockwork Masonry Columns.” *Can. J. Civ. Eng.*, 31(6), 1012-1023.

Köksal, H. O., Karakoc, C., and Yildirim, H. (2005). “Compression Behavior and Failure Mechanisms of Concrete Masonry Prisms.” *Journal of Materials in Civil Engineering*, 17(1), 107-115.

Kwasniewski, L. (2013). "Application of Grid Convergence Index in FE Computation." *Bulletin of the Polish Academy of Sciences*, 61(1), 123-128.

Lampropoulos, A.P., Tsioulou, O.T., and Dritsos, S.E. (2003). “Analytical Prediction for the Capacity of Old-New Concrete Interfaces.” *WIT Transactions on the Built Environment*, 72(1), 1-10.

Ling, F. Y. Y., Chan, S. L., Chong, E., and Ee, L. P. (2004). “Predicting Performance of Design-build and Design-bid-build Projects.” *Journal of Construction Engineering and Management*, 130(1), 75-83.

Lohr, J.R. (1992). “Evaluation of “Formwall”: A Post-Tensioned Dry-Stacked Masonry System.” *M.S. thesis*, The Pennsylvania State University, PA.

Mahboubi, A., and Ajorloo, A. (2005). "Experimental Study of the Mechanical Behavior of Plastic Concrete in Triaxial Compression." *Cement and Concrete Research*, 35(1), 412-419.

Marzahn, G. (1997). "Dry-Stacked Masonry in Comparison with Mortar Jointed Masonry." *Liepzig Annual Civil Engineering Report 2,* 353-365.

Molnár, M., and Jönsson, J. (2012). "Bending Capacity of Dry-Stacked Lightweight Concrete Block Masonry." *Proceedings of the 15th International Brick and Block Masonry Conference*, Florianópolis, Brazil.

Murray, E.B. (2007). "Dry-Stacked Surface Bonded Masonry – Structural Testing and Evaluation." *M.S. thesis*, Brigham Young University, UT.

Ngowi, J.V. (2005). "Stability of Dry-Stack Masonry." *Ph.D. thesis*, University of Witwatersrand, Johannesburg, South Africa.

Okail, H., Abdelrahman, A., Abdelkhalik, A., and Metwaly M. (2016). "Experimental and Analytical Investigation of the Lateral Load Response of Confined Masonry Walls." *HBRC Journal,* 12(1), 33-46.

Park, R. (1988). "Ductility Evaluation from Laboratory and Analytical Testing." *Proceedings of 9th World Conference on Earthquake Engineering*, Auckland, New Zealand.

Pave, R.F. (2007). "Strength Evaluation of Dry-Stack Masonry." *M.S. thesis*, University of the Witwatersrand, Johannesburg, South Africa.

Radaman, O.M., Abdelbaki, S.M., Saleh, A.M., and Alkhattabi, A.Y. (2009). "Modeling of Reinforced Concrete Beams with and without Opening by Using ANSYS." *Journal of Engineering Sciences*, 37(4), 845-858.

Roache, P.J. (2009). *Fundamentals of Verification and Validation*. Hermosa Publishers, NM.

Prabhu, S., Atamturktur, S., Brosnan, D., Dorrance, R., and Messier, P. (2014). “Foundation Settlement Analysis of Fort Sumter National Monument: Model Development and Predictive Assessment.” *Engineering Structures (Elsevier),* 65(1), 1-12.

Safiee, N.A., Jaafar, M.S., Alwathaf, A.H., Noorzaei, J., and Abdulkadir, M.R. (2011). “Structural Behavior of Mortarless Interlocking Load Bearing Hollow Block Wall Panel under Out-of-Plane Loading.” *Advances in Structural Engineering*, 14(6), 1185-1196.

Sayed-Ahmed, E.Y., and Shrive, N.G. (1996). “Nonlinear Finite-Element Model of Hollow Masonry.” *J. Struct. Eng.*, 10.1061/(ASCE)0733-9445(1996)122:6(683), 683-690.

Schwer, L. (2008). "Is Your Mesh Refined Enough? Estimating Discretization Error Using GCI." *7th LS-DYNA Anwenderforum,* Bamberg, I-I-45-54.

Sekender, A., and Page, A. (1988). “Finite Element Model for Masonry Subjected to Concentrated Loads.” *J. Struct. Eng.*, 114(8), 1761-1784.

Tavárez, F.A. (2001). “Simulation of Behavior of Composite Grid Reinforced Concrete Beams Using Explicit Finite Element Methods.” *M.S. thesis*, University of Wisconsin – Madison, WI.

Thanoon, W.A., Jaafar, M.S., Kadir, M.R., Ali, A.A., Trikha, D.N., and Najm, A.M. (2004). “Development of an Innovative Interlockig Load Bearing Hollow Block System in Malaysia.” *Construction and Building Materials*, 18(1), 445-454.

Uzoegbo, H.C. (2001). “Lateral Loading Test on Dry Stack Interlocking Block Walls.” *Structural Engineering, Mechanics and Computation*, 1, 427-436.

Uzoegbo, H.C., and Ngowi, J.V. (2004). “Lateral Strength of Dry-Stack Wall System.” *Journal of the British Masonry Society*, 17(3).

Uzoegbo, H.C., Senthivel, R. and Ngowi, J.V. (2007). “Load Capacity of Dry-Stack Masonry Walls.” *The Masonry Society Journal*, 25, 41-52.

Van Buren, K., Atamturktur, S., and Hemez, F. (2014). “Model Selection through Robustness and Fidelity Criteria: Modeling the Dynamics of the CX-100 Wind Turbine Blade.” *Mechanical Systems and Signal Processing*, 43(1), 246-256.

Vargas, H.G. (1988), "Mortarless Masonry: The Mecano System", *International Journal for Housing Science and Its Applications*, 12(2), 145-157.

Wight, J.K., and MacGregor, J.G. (2011). *Reinforced Concrete: Mechanics and Design*. Prentice Hall, NJ.

Willam, K., and Warnke, E. (1974). "Constritutive Model for the Triaxial Behavior of Concrete." *Proc. Seminar on Concrete Structures Subjected to Triaxial Stresses,* Int. Association of Bridge and Structural Engineering, Zurich, Switzerland.